J A D E

Proposal for a Compact Magnetic Detector at PETRA

D.P. Barber, J. Dainton, and R. Marshall
Daresbury Laboratory

W. Bartel, Th. Canzler, D. Cords, P. Dittmann, R. Felst,
E. Gadermann*, M. Helm*, H. Krehbiel, J. Olsson,
L.H. O'Neill, A. Petersen*, D. Pandoulas,
M. Schädlich*, and P. Steffen
DESY, Hamburg

P. Brauel*, G. Grindhammer, W.D. Kollmann, and K. Sauerberg*
II. Institut für Experimentalphysik der Universität Hamburg

W. Farr, B. Granz, J. Heintze, G. Heinzelmann, R.D. Heuer*,
P. Lennert, H. Rieseberg, A. Wagner, and A.H. Walenta
Physikalisches Institut der Universität Heidelberg

D. Darvill, F. Foster, and G. Hughes
Physics Department, University of Lancaster

J. Allison, B. Dickinson, F.K. Loebinger, P.G. Murphy,
and K. Stephens
Physics Department, University of Manchester

M. Imori, T. Kobayashi*, S. Komamiya*, M. Koshiba, S. Orito,
A. Sato*, T. Suda, Y. Totsuka, S. Yamada, and C. Yanagisawa*
High Energy Physics Laboratory and Department of Physics,
University of Tokyo

---

*graduate student

Spokesman R. Felst

Representatives of the groups:

Daresbury, Manchester Lancaster	R. Marshall
DESY, Hamburg	W. Bartel
Heidelberg	J. Heintze
Tokyo	S. Orito

Abstract

We propose an experiment which will be ready to take data from the first colliding beams at PETRA. The apparatus consists essentially of a system of cylindrical drift chambers placed inside a thin normal conducting solenoid. A modular array of leadglass shower counters surrounds the coil and beyond this we have a muon filter system. A small angle double tagging system is provided as a luminosity monitor and for two photon physics.

Using this apparatus we intend initially to explore the following physics:

1) Total annihilation cross section $e^+ + e^- \rightarrow$ hadrons.
2) Search for new particles by detecting weak decays to $e^{\pm}$ or $\mu^{\pm}$.
3) Check on Q.E.D. processes at high momentum transfers and search for neutral weak current effects in $e^+ + e^- \rightarrow \mu^+\mu^-$ and $e^+ + e^- \rightarrow$ hadrons.
4) Study of hadronic final states.
5) Survey of two photon initiated reactions.

Contents

1 PHYSICS AIM AND CONCEPT OF THE DETECTOR

1.1 Introduction

The advent of PETRA will open up a new domain of high energy physics. There are many important questions to be answered in this new region including:

What is the magnitude and the energy dependence of the total annihilation cross section?

Are new degrees of freedom (heavy hadrons and/or leptons) excited in this energy range?

What is the magnitude of electromagnetic-weak interference?

Does QED theory hold at high momentum transfers?

The answers to these questions will have a very profound impact on our understanding of elementary particles and their interactions. Our present understanding of particle physics may prove inadequate, and totally unexpected new phenomena may occur.

The experiment which we propose explores this new region. It is also designed to perform efficient and accurate measurements of such fundamental processes as $e^+e^- \to$ hadrons, e^+e^-, $\mu^+\mu^-$, and $\gamma\gamma$. A large solid angle and good lepton identification are therefore essential.

1.2. Detector

Some of the concepts of the detector have already been discussed at the Meeting on PETRA Experiments at Frascati (1,2). It consists of a large solid angle magnetic detector together with lead glass shower counters and a muon filter.

The layout of the detector is shown in figs. 1.1 and 1.2. A uniform axial magnetic field of about 5 kG will be generated by a thin ($\simeq 0.7\ X_o$) warm solenoid of diameter 1.9m and length 3.5m. The inner

detector will contain cylindrical drift chambers. These chambers (1) are expected to provide a double track resolution of about 3mm and about 50 samplings will be performed along each track. This dense sampling is essential for pattern recognition, for the detection of V-particles, and for ionisation measurements which we will attempt to use for particle identification at high energies.

Test results indicate that a spatial resolution of ±100μm/sampling can be expected from these chambers. The resulting momentum resolution is shown in fig. 1.3. This can be improved by taking into account information about the interaction point and will be adequate for the proposed measurements. As fig. 1.3 indicates we have a momentum resolution of ± 10% at 15 GeV/c which means there will be no difficulty in measuring the charge of $\mu^+\mu^-$ to the highest energies available at Petra.

Outside the coil a system of lead glass counters will be used to measure γ ray energies and to identify electrons. This is expected to provide a shower energy resolution of $\pm 6\%/\sqrt{E}$ (E in GeV) and a hadron rejection factor of 500. There will be a muon filter with total thickness equivalent to 6 absorption lengths sampled with planar drift chambers. This serves to filter out hadrons to the level of 2×10^{-3}.

Beam pipe- and time-of-flight-hodoscopes will be installed inside the coil. A clean and unbiased trigger will be obtained using these hodoscopes, the fast energy information from the lead glass counters, and a fast track finding logic. We plan to install a system of shower detectors at small angles to tag electrons from photon-photon processes and to monitor the luminosity.

1.2 Physics aim

With the apparatus, we plan the following measurements:

1) Measurement of the total annihilation cross section:

This is a very fundamental measurement and should be performed at an early stage. A high value of $R = \sigma(e^+e^- \to \text{had})/\sigma_{\mu\mu}$ could be an indication of something new happening in the Petra energy range. Structures (spikes, bumps, shoulders, etc.) in the total cross-section could indicate that new degrees of freedom are being excited. The large solid angle of the apparatus and the proposed trigger mode will provide an efficiency close to 100% for annihilation events, $e^+e^- \to$ hadrons. The measurement of the charged particle momenta and γ-ray energies allows good discrimination against photon-photon reactions on the basis of the total observed energy. Therefore we should be able to perform an efficient and accurate measurement of the cross-section $e^+e^- \to$ hadrons.

2) Search for new particles:

Clear signals of new weakly decaying particles could be obtained by detecting $e^\pm$ and/or $\mu^\pm$ in the final states. For example pair-produced heavy leptons must have significant branching ratios into the final states $e^\pm+\nu+\nu+$hadrons, $\mu^\pm+\nu+\nu+$hadrons, and $e^\pm+\mu^\mp+$neutrinos (3). A pair of new hadrons can be searched for in the channels $e^\pm\nu+$hadrons, $\mu^\pm\nu+$hadrons, and $e^\pm\mu^\mp+$hadrons+neutrinos. An increase of the annihilation cross-section together with a corresponding increase of these leptonic or semileptonic final states could provide clear evidence for a new heavy particle. With our apparatus, electrons and muons can be detected even in events containing many hadrons. The observation of such $e\mu+$hadrons events would indicate that the new particle is a hadron. On the other hand "$e\mu$ + missing energy" events would point towards a

new lepton. Thus a solid angle close to 100% is essential in order not to miss the hadrons or leptons from reactions of the type $e^+e^- \to e^+e^-\mu^+\mu^-$.

3) Search for electromagnetic-weak interaction interference effects :

The existence of a weak neutral current has been established by recent neutrino experiments. However, whether the neutral current couples to e^+e^- and $\mu^+\mu^-$ has yet to be established. If it does, the value and the type of the coupling must be investigated. The reaction $e^+e^- \to \mu^+\mu^-$ is well suited to these investigations. Interference between the weak and the electromagnetic currents should show up as a forward-backward asymmetry of the μ^+ or μ^-. Once the effect of the weak interaction is observed, we can investigate the combined structure of weak and electromagnetic interactions by performing accurate measurements of $e^+e^- \to e^+e^-$ and $\mu^+\mu^-$ processes over a large angular- and energy-range.

If the colliding beams are transversely polarized the electromagnetic amplitude will be suppressed in the vicinity of $\theta \sim 90^\circ$ and $\phi \sim 90^\circ$, resulting in an enhancement of the interference effect. Therefore we need real time monitoring of the beam polarization, which can be obtained using the purely electromagnetic process $e^+e^- \to \gamma\gamma$. In addition this reaction provides an independent check of the validity of the electron propagator in QED.

4) Study of hadronic final states:

Apart from the total cross-section measurements we plan to investigate the structure of the hadronic final states in more detail. As explained later, it will not be difficult to prove the existence or non-existence of jets.

K_S and Λ can be identified by reconstructing the invariant mass

of the decay products and their vertex, and $\pi^{\pm}/K^{\pm}$ can be separated by time-of-flight up to 600 MeV/c. In addition we will attempt to separate particles in the GeV region by measuring dE/dX with the drift chambers.

5) Survey of photon-photon processes

A tagging system at small angles will serve as a luminosity monitor and together with the central detector it will provide the possibility of studying the production of C = +1 final states, and of examining the structure of the photon by deep inelastic electron-photon scattering.

References

1) University of Tokyo Group, presented by S. Orito
Discussion Meeting on PETRA Experiments, Frascati (1976), page 643

2) DESY Heidelberg Group, presented by J. Heintze,
Discussion Meeting on PETRA Experiments, Frascati (1976), page 660

3) For example, Y.S. Tsai, Phys. Rev. D, 4 (1971) P 2821

Figure Captions

Fig. 1.1 Radial section through one quarter of the apparatus

Fig. 1.2 Transverse section of the apparatus

Fig. 1.3 Momentum resolution obtained for π's from drift chambers without assuming any knowledge of the interaction point

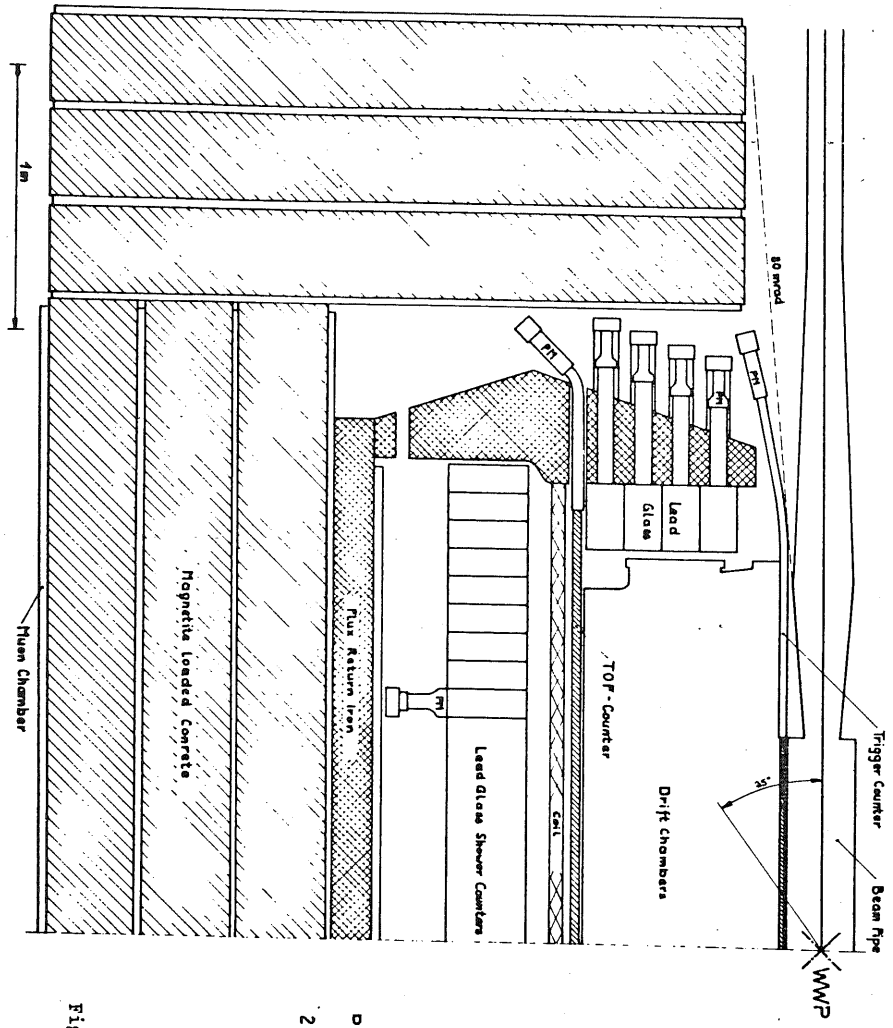

Fig. 1.1

DESY
25159

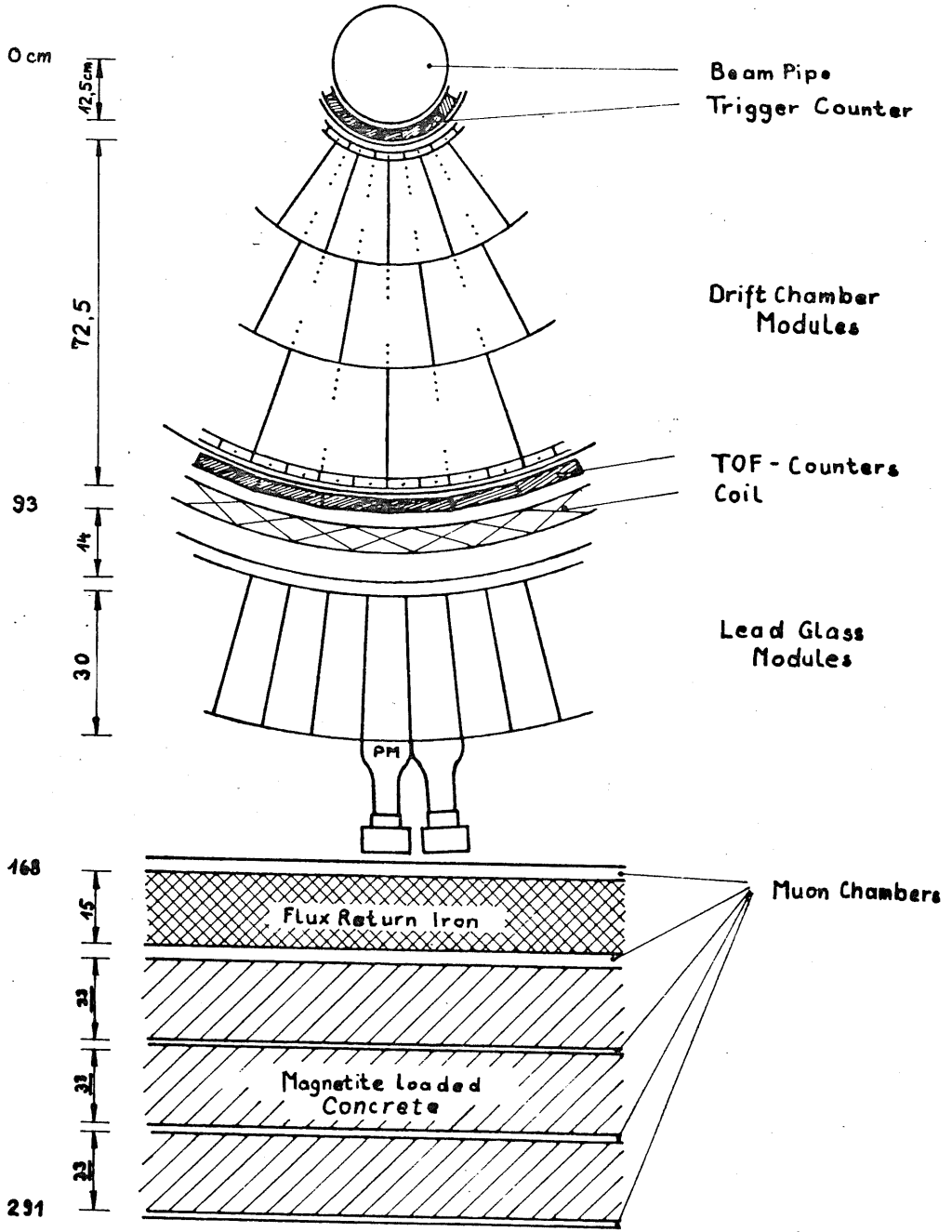

Fig. 1.2

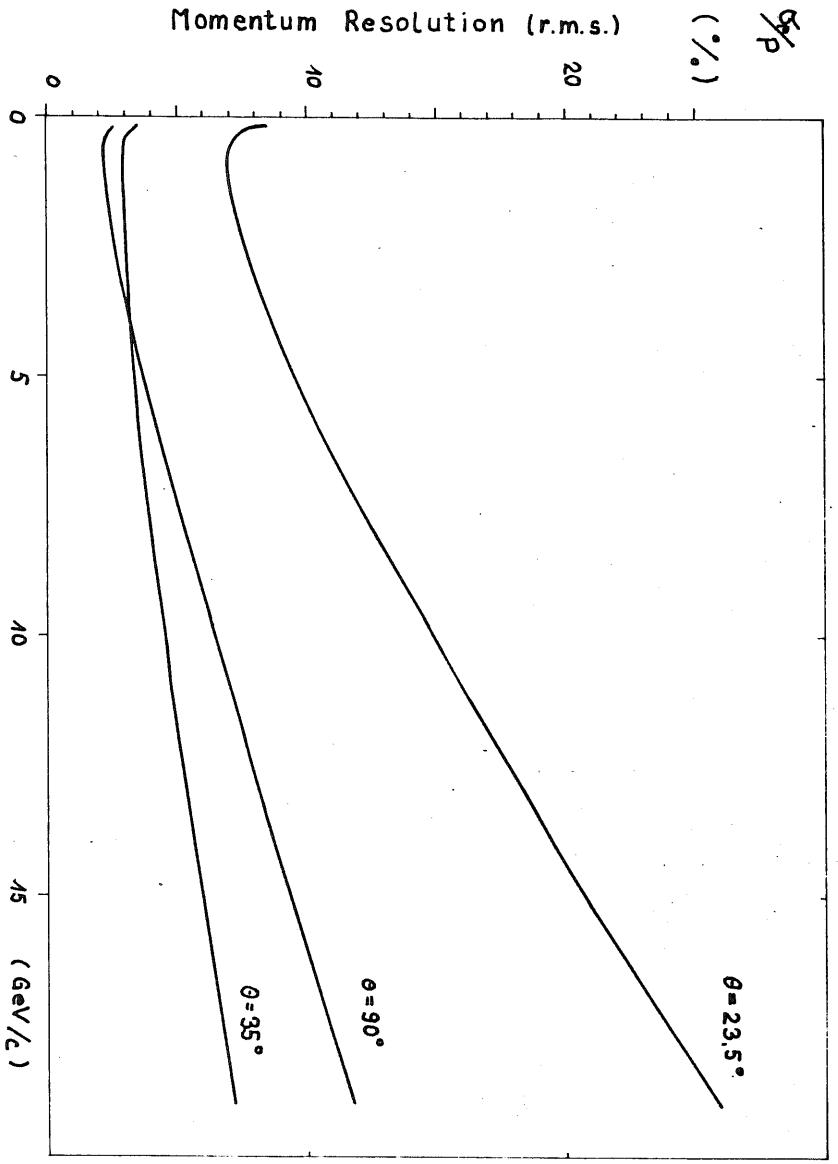

Fig. 1.3

2 APPARATUS

2.1 Beam Pipe Design

The beam pipe for our experiment has to meet certain boundary conditions which are imposed by the machine operation, the detector itself and the requirement to shield it against synchrotron radiation.

The most important constraints are the following:

1) The inner diameter of the beam pipe in front of the first quadrupole after the intersection point has to be 22cm to accomodate different beam optics. This does not exclude an adjustable collimator which can be closed to about 4 cm from the beam axis for the present optics.
2) Sharp edges in the beam pipe should be avoided to minimize RF losses. Before the actual beam pipe is built the losses should be determined experimentally using a model.
3) The central part of the beam pipe should allow for particle detection through a thin window in the angular range $10^{o} \leq \theta \leq 170^{o}$. A window for the tagging system should be provided between 100 and 30mrad.
4) No direct synchrotron radiation originating from the second quadrupole and the weak (16%) bending magnet should hit the beam pipe.

One of the main worries when surrounding the interaction region with detectors is that synchrotron radiation might saturate the chambers and scintillation counters. The best means of keeping the level of synchrotron radiation low is to design the beam pipe in such

a way that at least two scatters off "high Z" material must occur before the radiation can enter the detectors.

A possible beam pipe design is sketched in fig. 2.1. The central part consists of a 2 - 3mm aluminium pipe 25cm in diameter and 1.6m long to allow for particle detection in the angular range $10^{o} \leq \theta \leq 170^{o}$. Absorbers are inserted at the end flanges to reduce the effective solid angle for synchrotron radiation scattering towards the inner detector. Thin steel windows between 30 and 100mrad serve the tagging and luminosity monitor systems. Towards the first quadrupole the pipe widens from 15 to 22cm in diameter. Wherever possible the pipe is surrounded by lead reinforced with steel, the resulting weight necessitates rather careful design of a stable support structure. A total of four vacuum pumps, two on each side of the interaction region, will provide a vacuum of 10^{-10} torr. Since the beam pipe has to be baked out after installation two or four bellows will be included in the final construction.

A forty radiation length thick adjustable tungsten collimator placed in front of the first quadrupole shields against primary synchrotron radiation and high energy electrons and positrons in the beam halo. This collimator will also be the main source of synchrotron radiation backscattered from the surface facing the intersection.

The reduction factor for secondary synchrotron radiation entering the central detector resulting from double scattering and favourable geometry is estimated to be of the order of 10^{-10}. At a beam energy of 15 GeV and 20 mA current there are a few times 10^{14} photons per second passing through the tungsten collimators so that there will be approxi-

mately 10^{5} photons per second hitting the detector (We have taken the cut-off energy for photons to be 20 keV). If necessary additional shielding can be installed in the form of thin tantalum sheets surrounding the interaction point.

2.2 Solenoid Magnet

We propose to build a normal conducting, thin walled solenoid which will provide a uniform field of 5 kG throughout a cylindrical volume of 1.9m diameter and 3.5m in length.

The choice of a normal as opposed to a superconducting magnet was motivated by the cost, ease and time scale of construction together with the need to avoid the problems associated with operating the high resolution drift chambers within a high magnetic field.

It is essential that there should be as little material as possible between the interaction region and the lead glass shower counters which are situated immediately outside the coil of the magnet, otherwise the resolution of the shower counters would be adversely affected. The magnet has therefore been designed to have a coil with thickness ~ 0.5 of a radiation length (X_o). This requirement means that the coil conductor must be made of aluminium and not copper.

To provide a field of 5 kG throughout the cylindrical volume, a total of $1.4*10^{6}$ amp turns are required and for an aluminium coil, there is then a unique relation between the power dissipation, P (MW) and the thickness t (X_o),

$$P = \frac{1}{1.1\ t}$$

The optimum design is a compromise between a desire for low power (but which means large t) and the need for a thin coil (which means large power). An operating power of 2.0 MW and an associated coil thickness of 0.46 X_o have been chosen as design figures since we regard both values as acceptable. The addition of insulation material and heat shields will increase the thickness slightly to $\sim 0.5\ X_o$.

From the point of view of cost and convenience, it is desirable to use an existing power supply. A variety of power supplies capable of providing a minimum of 2.5 MW have been considered, with current outputs ranging from 1500 to 8000 Amps.

Since a low current power supply means a large number of turns in the magnet coil, and is associated with a complex cooling water circuit (typically a hundred high pressure water connections along the length of the coil), we prefer to build a magnet which is powered by the highest possible current source.

The proposed coil winding configuration is shown in fig. 2.2. There are two layers and each layer is wound with five starts. A single layer therefore consists of a five-fold wrap of 20 turns. The ten windings of 20 turns each are then connected electrically in series at the ends of the coil. As far as water is concerned however, the ten windings are operated in parallel. There are several advantages of this arrangement. The aluminium conductor is required in ten pieces each no more than 120m in length. It is therefore not necessary to make any potentially unreliable joints within the coil itself. In addition, all the water and electrical connections are at the ends of the coil. In fact the conductor can be wound in such a way that it can be fed out

through the return yoke at each end. Both the electrical and water connections can then be made at a point where they are readily accessible. The danger of a water leak inside the detector is thus eliminated.

A heat shield will be provided on the inside and outside of the coil in order to thermally isolate the coil region from the shower counters and the inner detector. The shield will be either a water cooled 1mm thick aluminium cylinder or an air cooled epoxy cylinder of similar size.

The coil windings will be built as a rigid structure without any additional cylindrical support. It will be supported at each end by the circular end caps of the return yoke. The return yoke itself which forms the first layer of the muon filter, consists of a soft iron cylinder of diameter 3.8m and wall thickness 15cm. The circular end caps will each be made of two shaped interconnecting annuli. The outer annulus covers the region from the coil to the return yoke and is also used to support the weight of the cylindrical yoke and the coil. The inner annulus covers the region with radius smaller than the coil. It will be removable to allow the whole of the inner detector to be slid in and out without dismantling coil or shower counter assembly. The iron end caps will also contain holes to allow access for power and water connections, for the signal and EHT cables for the shower counters and for the end cap shower counters themselves.

The parameters of the magnet and power supply are summarised in the Table below.

Magnet	Conductor material	Aluminium
	Average wall thickness of coil	0.5 X_o
	No. of turns	200
	Winding configuration	2 layers of 5
	Water circuits	10
	Water flow	10 l/sec
	Water pressure	6 atmospheres
	Water temperature rise	50°C
	Nominal power	2.0 MW
Power supply	(Brentford)	
	Input requirements	11 kV, 50 Hz, 160 A
	Output	0-312 V, 0-8000 A
	Stability	0.05%
	Water flow	114 l/min
Components -	Oil booster transformer (outdoor)	18 t
	Voltage regulating transformer (")	14.5 t
	Rectifying transformer (indoor)	9.2 t
	Rectifying unit (indoor)	5.1 t

2.3 The Internal Detector

1) Introduction to this device

The purpose of this device is to detect charged particles whilst maintaining an insensitivity to photons. It should identify tracks of particles from complicated interactions and measure their directions and curvatures. We intend to make a detector which is capable of analysing a narrow jet structure and which can to some extent also

identify types of particle. The system is based on the "jet chambers" proposed at the recent Frascati meeting (1).

In this section we explain the principle of jet chambers and describe the structure of the internal detector. The performance of the system is described on the basis of experimental tests carried out recently on suitable prototype modules. A much more detailed description of the mechanical and electronic characteristics of these new detectors is given in the Appendix to this proposal.

2) Principles of jet chambers

The"jet chamber" is a drift chamber with large drift spaces and is provided with a special read out electronics. This is shown schematically in fig. 2.3. For each track passing through the chamber three signals are recorded:

T_i is a timing signal indicating the drift time associated with track i,

A_i^r is the signal amplitude from track i which is recorded at the right hand end of the anode wire,

A_i^l is the corresponding amplitude recorded at the left hand end.

The three signals from track i appear almost simultaneously (i.e. within a few ns) and can be uniquely correlated with each other. T_i and $(A_i^r - A_i^l)/(A_i^r + A_i^l)$ give both coordinates for each particle whilst $(A_i^r + A_i^l)$ is a measure of the energy loss.

When several chambers of this type are arranged behind each other a geometrical reconstruction of a jet of particles should be possible.

In addition the mass can be determined from dE/dx measurements by sampling many times the energy loss of each particle.

3) Description of the internal detector

The design of the internal detector is shown in fig. 2.4 and 2.5. It consists of 5 cylindrical jet chambers. Chambers 1 and 5 are single layer jet chambers similar to the chamber shown in fig. 2.3. Since the chambers are operated in an axial magnetic field of 5 kG, the field generating potential wires have to be connected to the high voltage in such a way that the Lorenz-force is compensated (2). Chambers 2 - 4 are multilayer jet chambers. Each chamber consists of 24 cells and the details of one cell are shown in fig. 2.6. In principle such a cell consists of 16 chambers of the type shown in fig. 2.3 placed one after the other. The drift field is generated between the metallized mylar sheets S and the anode wires A and potential wires P_o. The equipotential planes are parallel to the sheets S. If the sheets S are assumed to be at ground potential point (1) is at a potential $U_1 = E \cdot d_1$ and point (2) is at $U_2 = E \cdot d_2$ (E being the drift field). Linear potential drops between S and points (1) and (2) are accomplished by means of the control potential wires P_1 and P_2.

The row of anode wires A and potential wires P_o is connected to a linearly dropping potential between points (1) and (2) to produce a constant drift field. In addition a counting voltage U_a of a few kilovolt is applied between the anode and potential wires in order to achieve the necessary gas amplification.

The ionization of a particle crossing the chamber is collected at the anode wires. In the absence of a magnetic field the drift spaces

belonging to each anode wire would be separated by planes normal to the sheets S as indicated by the dashed lines in fig. 2.6. In the presence of a magnetic field the domains belonging to one anode wire are twisted as indicated by the hatched region in fig. 2.6. A twisting angle of 4.5^o is obtained with B = 5 kG, E = 3000 V/cm and a drift velocity v_D = 5cm/µs.

A similar arrangement of electrodes, but with parallel geometry, has been suecessfully operated by W.W.M. Allison et al. as a prototype of the particle identification device ISIS (3).

The parameters of the chamber system are compiled in the following table :

Chamber	No. of wires/cells	Total No. of wires	radius (cm)	lenth of wires (cm)	average length of drift space (cm)
1	1/24	24	18	150	2.3
2	16/24	384	19 - 40	240	3.9
3	16/24	384	40 - 61	240	6.6
4	16/24	384	61 - 82	240	9.4
5	1/48	48	83	240	5.4
		1224			

Electronics capable of encoding 8 triplets of pulses T_i, A_i^r, A_i^l will be connected to each wire. The analysis of multiprong events will be based on this information. In addition, special electronics capable of measuring very accurately the drift time of one particle will be

connected to each wire of chambers 1 and 5 and to the middle wires of chamber 3. This will give improved coordinate accuracy for events with low track multiplicity and will also check the electronic system.

The whole set of chambers is contained in a pressure vessel which enables us to use a 75% propane/25% ethylene mixture as a counting gas at a pressure of 4 atm. Test measurements show that this gas mixture yields a very good spatial resolution and good accuracies for the dE/dx measurement. Alternatively, the chambers can be operated with the same gas mixture at atmospheric pressure or with an argon/isobutane mixture.

Further details of the mechanical construction and of the electronic system are described in the Appendix.

4) Expected performance of the internal detector

As outlined at the Frascati meeting (1) we expected an improved performance of the internal detector if a molecular gas at a pressure of a few atmospheres is used in place of the conventional argon isobutane mixture. Experimental tests in this direction have meanwhile been performed, and some of the results are included in the following discussion.

Spatial resolution (ϕ-coordinate)*

The ϕ-coordinate is directly measured by the drift time. In order to investigate the resolution obtainable in drift spaces of a few cm length with various gases three chambers of the type shown in fig. 2.3 were arranged in layers and placed in a pressure vessel. The length of the drift spaces was 5cm and the mechanical precision was about 10μ. The test

* We use polar coordinates with z-axis along the beam direction.

was performed at the Bonn Synchrotron using a narrow beam of 1 GeV electrons, directed normally to the drift planes. The spatial resolution as a function of the length of drift path is shown in fig. 2.7 for various gases. Best results were obtained with a mixture mixture of 25% ethylene (C_2H_4) and 75% propane (C_3H_8) at a pressure of 4 atm. This is due to the low diffusion and the high ionization density in this gas mixture. A spatial resolution σ_ϕ<50μ is obtained with 5 cm drift path. A drift field E of 3kV/cm was used and at this value the drift velocity was found to be nearly independent of the ratio E/P (P=pressure).

With the "high precision electronics" described in the preceding section a spatial resolution of about $\sigma_\phi \simeq 50\mu$ should be obtainable, but with the "jet chamber readout electronics" the precision is limited by the accuracy of the time measurement to about 100μ.

Spatial resolution (z-coordinate)

The z-coordinate is measured by the charge division method. We have made some tests of this method using a 20μ tungsten wire of 2.5m length mounted in a cylindrical counting tube. Low impedance amplifiers ("VV 69" described in the Appendix) were connected at both ends of the wire. Fig. 2.8 shows the amplitudes recorded for various injection points of the radiation from a Fe^{55} source. The two dimensional display of the two amplitudes is shown in fig. 8a. From this diagram a spatial resolution of the z-coordinate

$$\sigma_z \sim 2 \text{ cm}$$

can be estimated. The estimate is valid also for passing particles because

of the large specific energy loss obtained in the propane/ethylene mixture at 4 atm.

The z-resolution discussed so far refers to the measurement of one single wire. Since we have 50 wires along one track we expect about a 7-fold improvement in z-resolution.

An independent measurement of the z coordinate is obtained by the "high precision electronics". Since the propagation time of the signals along the wire is 12.5ns, a digitisation with 1ns bins results in a z resolution $\sigma_z \simeq$ 6cm. This measurement can be used for calibration and control.

Double pulse resolution (ϕ-coordinate)

The double pulse resolution depends on the amplifier and discriminator system since the pulses in a jet chamber are in general very smooth and narrow. Using the propane/ethylene gas mixture at 4 atm. a rise time of 5ns and a fall time of 20ns was observed. With the existing amplifier/discriminator system (which has to be slightly modified in order to enable us to perform pulse height measurements) a time resolution of 100ns for double pulses corresponding to 5mm in space is easily obtained. We hope to reach with an improved system a double pulse resolution of 50ns which corresponds to 2.5mm in space.

Double pulse resolution (z-coordinate)

Since the z-coordinate is measured independently on each track the double pulse resolution of the z-coordinate is in principle not limited. However, the coordinates of two tracks cannot be measured if both tracks

are within the double pulse resolution of the ϕ-coordinate. This will happen only along short sections of such tracks unless the two particles have the same sign of charge and momentum.

Response to inclined tracks and double pulsing

The response of a chamber to tracks which are inclined in the θ direction is complicated only by the fact that the avalanches are spread over varying lengths of wire (at $\theta = 90^{\circ}$ the spread is of course minimal). This does not interfere with the operation of the chamber. Tracks deviating from the radial direction in the azimuthal view by appreciable angles may cause double pulses since the differences in the times of arrival of different ionization clusters may exceed the double pulse resolution in ϕ. Such angles will occur, however, only for particles with momenta below 150 MeV/c or for large angle decay products of particles decaying in the chamber. Another source of possible double pulsing is the passage of a particle close to a counting wire. The maximum difference in the time of arrival of an ionization cluster in this case is 100ns (= 5mm). It should be noted that both types of double pulses are reduced when the pressurized propane/ethylene mixture is used because of the dense ionization along the tracks. We do not expect double pulses to be a serious problem in pattern recognition.

Measurement of the ionization loss

A measurement of the ionization loss can be used for the determination of the particle velocity and then in conjunction with a momentum measurement for the determination of the particle mass. Because of the statistical

fluctuations of the ionization loss a sampling of many measurements is necessary in order to reach the required precision. This is discussed extensively elsewhere (3,4,5).

The full width of the energy loss distribution decreases with increasing sample thickness and pressure and also decreases with decreasing mean ionization potential. For example the width for 1cm of propane/ethylene at 4 atm. is 30% and this corresponds to 25cm of argon at 1 atm.. The resulting precision of a dE/dx measurement from 48 samplings in the pressurized propane/ethylene is expected to be about 6% FWHM. With such a resolution, π/K-separation is possible below p = 0.7 GeV/c. At higher momenta the separation depends on the relativistic rise in the counting gas, and there is no direct information on this for propane/ethylene at 4 atm.. Comparing the calculated data for argon and methane at atmospheric pressure (5) and extrapolating to the propane/ethylene mixture at 4 atm., we expect that a π/K - separation will be possible in the momentum range of 2 - 7 GeV/c. An experimental investigation of the relativistic rise in a propane/ethylene mixture is in preparation.

Magnetic deflection, multiple scattering and spatial resolution

In fig. 2.9 we compare the spatial resolution σ_ϕ with the magnetic deflection sagitta S_M and the sagitta due to multiple scattering σ_{sc}. A magnetic field of 5 kG and a track length of 65cm corresponding to the radial distance between chambers 1 and 5 are assumed. The total radial thickness between the chambers 1 and 5 will be less than 1.4% of a radiation length out of which 0.9% is due to the counting gas

(propane/ethylene mixture at 4 atm.). Fig. 2.9 shows, that we can expect a momentum resolution $\frac{\Delta p}{p}$ of $\pm$ 2 to 3% up to 5 GeV/c and of about $\pm$ 12% at 20 GeV/c.

Calibration

The calibration of the internal detector can be checked continuously in several ways. Firstly we can systematically follow the tracks of single cosmic ray particles; secondly we can compare the coordinates from the "jet chamber" read-out logic with those from the "high precision" electronics. In the low momentum regime velocity determinations from the dE/dx measurements may be compared directly with results from the time-of-flight counters. A regular calibration will also be available from either an electronic pulser or from X ray flash tubes.

2.4 The Trigger and T.O.F. Counters

In order to provide the essential charged particle fast trigger we intend to construct two layers of scintillation counters. The first is placed immediately around the pipe at a radius of about 14cm and the second just outside the inner detector pressure vessel at a radius of 90cm. The inner layer consists of 20 individual counters arranged parallel to the beam axis whilst the outer layer consists of 42 counters similarly aligned. The counters will be up to 3.5m in length so that it will be necessary to have photo-tubes placed at both ends and light guides passing through the iron end caps. It is proposed to use NE 110 scintillator material (or equivalent) and photo-tubes of the type RCA 8575 or Valvo 56 AVP

Time-of-flight "stop" signals are provided by the outer layer scintillation counters - the "start" signal being provided by the beam crossing time. Careful setting up of the electronic readout should then result in time measurements accurate to $\sigma \approx$ 0.3nsec. This will allow π-k separation up to a momentum of 600 MeV/c and p - k separation up to 1100 MeV/c.

2.5 Leadglass Shower Detector

This detector is designed to measure with good resolution the total energy of an electromagnetic shower resulting from a Q.E.D. process or from a component of some multihadron final state. It is also required to identify electrons positively.

The shower detector covers 94% of 4π solid angle and is segmented into 3048 blocks of leadglass each with a thickness corresponding to 12.7 radiation lenths and viewed from the back by a 3 inch diameter photo-tube. The signal amplitudes from each counter are recorded individually and are also simultaneously added linearly.

A fast trigger depending on the total electromagnetic energy is thus provided by the summed amplitude signal. This will be a simple way to eliminate unwanted background events which deposit little energy, and also provides the trigger for events with only neutral particles in the final state.

Those electrons which may be present in multihadron events can be identified by comparing the momentum measured by the magnetic detector with the shower energy of that track. A detailed and careful check on the ionization loss measured along the track by the drift chambers will improve the identification capability.

It must also be emphasized that the lead glass counter is a well established conventional detector. Little technical development is needed in order to build a tough, reliable and stable device.

Construction

The general arrangement of the leadglass blocks which are placed just outside the magnet coil and also inside the iron end caps is shown in fig. 1.1. The cylindrical part of the detector is segmented into 84 parts in the ϕ-dimension and 34 parts along the z-direction. In order to fit neatly together the blocks have a tapered shape: the front end is 8.5 x 10.7cm^2, the rear end is 10.7 x 10.7cm^2 and the depth is 30cm. The photo-tubes are attached to the rear end by means of an optically clear cement. Fig. 2.10 illustrates the method of supporting each module. Each of the end cap detectors consists of 96 identical blocks with a size of 14 x 14 x 30cm^3; they are fixed on the inside wall of the iron return yoke through which holes are drilled for the light guides.

The magnetic field strength at the photo-tubes is calculated to be less than 3 gauss at all locations so that magnetic shielding is possible using conventional techniques. The three inch tubes are selected for optimum gain stability over long periods of time; the type selected has a bialkali photo cathode with venetian blind dynode structure. We have checked that the gain of this type of tubes varies slowly, and the drift observed is typically 2-3% per year under actual experimental conditions (6)

Calibration

All the leadglass counter elements will be calibrated before installation using electron beams, and selected elements will be checked

for π-e separation using pion beams.

For real time monitoring of the gain of each element, we intend to use fast pulsed Xe flash lamps which emit an optical spectrum similar to the Čerenkov light in the leadglass. The light from each lamp is fanned out to about one hundred counters using optical fibre guides. In order to relate the outputs one fibre from each lamp goes to a common phototube looking at a stable standard light source made from a radioactive source embedded in a scintillator. Thus all the outputs are calibrated with respect to this standard light source.

Since the gain drift is expected to be smoothly and slowly, copious $e^{\pm}$ from various Q.E.D. processes ($e^+e^- \to e^+e^-$, $e^+e^-\gamma$, $e^+e^-e^+e^-$) can also be used for the calibration.

The whole counter system is monitored by the on-line computer which checks regularly the gain of each element.

Properties

The overall resolution for photons and electrons of the cylindrical part of the detector is expected to be $\Delta E/E = \pm 6/E^{1/2}$ % (E-GeV). This resolution has been achieved by several groups using similar modular leadglass arrays (7). For the end-cap detectors the resolution will be worse because of the relatively small light collection efficiency.

The energy resolution of the leadglass counters is somewhat reduced by the material (0.6 X_o mainly due to the coil) between the interaction point and the counters. This effect has been investigated with an electron test beam at various momenta. The results are summarized in fig. 2.11. The effect sharply decreases with electron momentum and can be neglected above 2 GeV, where the shower energy resolution is

important for the electron identification.

The angular resolution for photons will be about ± 20mr and pairs of electrons or photons must be separated by more than 140mr to give undistorted energy measurements. A pion rejection factor better than 300 is expected for momenta above 2 GeV/c.

2.6 The Muon Filter

1) Introduction

We have designed a rectangular muon filter to cover a solid angle of close to 4π sr (figs. 2.12,2.13,2.14). The filter itself has a thickness of 4 hadronic absorption lengths whilst the shower detectors and return yoke of the solenoid provide two further absorption lengths of material. Four layers of drift chambers are used to detect charged particles. Iron and iron-ore-loaded concrete have been considered for the absorbing material. Besides the obvious requirement of adequate discrimination against hadrons, important design considerations have been good access to the inner detector, good mechanical stability, simplicity and low cost.

2) Muons from pion and kaon decay

The decays $\pi^{\pm} \to \mu^{\pm}\nu$ and $K^{\pm} \to \mu^{\pm}\nu$ are an unavoidable background to muon identification. They have been discussed extensively by Carrol et al. (8) who found that a rough momentum measurement in the filter reduces the background by about a factor of 3. This, however, requires the provision of a magnetic field (obtained, for example, by using magnetised iron as the absorber) and greatly adds to the cost of construction and the complexity of the analysis. In order to meet deadlines and reduce costs we do not propose to provide such a field and as a consequence have been able to investigate the possibility of using a nonmagnetic material as the absorber.

It is still possible to eliminate a large fraction of $K^{\pm}$ decays by

angle measurement due to the relatively large Q-value. In this way, we estimate that the $K \to \mu$ background can be reduced to a level below the $\pi \to \mu$ background even though the kaons have a much higher decay probability.

The probability of pion decay is determined mainly by the length of the interaction-free region in the inner detector. The probability of penetrating the shower detectors and flux return yoke and subsequently decaying is small. For our apparatus the effective decay path is about 1.3m giving a $\pi \to \mu$ decay probability of 0.2% at 15 GeV/c.

3) Thickness of Filter

We require enough absorber to reduce the hadron punch-through probability to the level of the $\pi \to \mu$ decay probability or less. Engler et al. (9) and Harris et al. (10) have shown that with detectors giving either pulse height information or having multi-track capability, the experimental hadron attenuation length approaches the theoretical absorption length obtained from the hadron-nucleus total inelastic cross-section.

The shower detectors and flux return yoke provide over 2 absorption lengths of material and we propose to add another 4 absorption lengths giving a punch-through probability of approximately $e^{-6} = 0.2\%$ in a direction perpendicular to the beam. (In all other directions the effective thickness is greater giving an average value of about 8 absorption lengths).

4) The Detectors

We need several layers of detectors to aid hadron rejection and to permit track reconstruction so that a track in the muon filter can be

matched with a track in the inner detector where momentum is measured. We therefore propose 4 layers of detectors initially. The first layer will be placed between the shower detectors and the flux return yoke of the solenoid. Further layers will be placed between the return yoke and the filter and on the outside of the filter. The filter itself will be divided into 3 parts and a detector layer placed in one of the gaps.

We propose to use self-supporting drift chamber modules, 30cm wide, 2cm deep and up to 5m long with a single longitudinal signal wire. In the central region of the filter all modules will have their signal wires parallel to the beam direction. The signal wires in the end caps will be horizontal.

The readout electronics for each module will be capable of handling up to 4 signals per trigger with a track-track resolution of 1cm. We expect to be able to measure distances perpendicular to the wire to an accuracy of $\pm$ 2mm (standard deviation) and distances along the wire to an accuracy of $\pm$ 1% of the length of the wire using the charge sharing method. Thus, in the central region, we will achieve resolution better than the uncertainties due to multiple scattering ($\pm$ 1cm at 15 GeV/c) in the azimuthal coordinate ϕ but somewhat worse resolution in the longitudinal coordinate z. A good measurement of one coordinate should be adequate to match tracks with those of the inner detector and eliminate $K \to \mu$ decays in most cases. Also, with several layers of parallel wires it is easy to eliminate inefficiencies and left-right ambiguities.

The total number of drift chambers required for 4 layers of detectors is 540. Inclusion of a further layer at a later date would require a further 130 chambers.

5) Choice of Absorber

Rolled steel, cast iron and concrete have been considered as absorbers.

Rolled steel gives the most adaptable solution. It is however the most expensive.

Cast iron is probably the worst alternative. Its price comes between concrete and steel but it cannot be welded, machining may be difficult due to the presence of free iron carbide and dimensional inaccuracies and twists will be present due to uneven cooling.

Concrete is not as adaptable as steel but this is not a serious disadvantage as considerable experience exists in adapting concrete shielding. Shielding concrete (specific gravity 2.5) would be too bulky leading to the need for an excessive number of detectors. However an iron-ore-loaded concrete could have an absorption length not much larger than iron. The possibility of obtaining large quantities of magnetite-loaded concrete having a specific gravity of 4.8 is still being investigated. It would have an absorption length of 25cm (compared with 17.1cm for iron). A comparison of iron and magnetite-loaded concrete filters is made in the following table :

Comparison of Iron and Magnetite-Loaded Concrete

	Iron	Concrete
Specific Gravity	7.9	4.8
Absorption Length (gm cm^{-2})	135	120
Absorption Length (cm)	17.1	25.0
Thickness of Absorber (m)	0.68	1.00
External Dimensions of Filter (m^3)	5.6 x 6.05 x 6.95	6.45 x 6.76 x 7.75
Mass of Absorber (t)	1000	960

One suggestion is to encapsulate the loaded concrete within a sheet steel box. This has the advantage that the slabs will be accurate to size and no reinforcement bars or special moulds will be required. The cost of the concrete absorber alone would be less than half the cost of an equivalent iron absorber.

6) Overall Design

The basic design of the filter is substantially the same whatever the construction material. The size of components can be limited to 20 t to suit the capacity of the cranes at DESY. All components will be attached to one another so that no part relies solely on gravity to maintain its position.

Good access to the inner detectors has been an important design consideration. Therefore we propose to attach roller skates to each section

allowing movement perpendicular to the beam. The skates will run on steel plates inserted in the floor. In parting the filter to obtain access to the inner detector, care has to be taken to ensure that each sub-assembly is stable as a structure and that the base is sufficiently large to resist toppling.

The inner detector is supported by the base B of the filter. In normal running conditions access to the inner detector will be available through the port shown in one of the end plates. All services for the inner detector will enter through a similar port in the end plate. Better access can be obtained by removing a side wall A (fig. 2.12). For access by crane to the inner detector it will be possible to remove one or both of the bridge section C (figs. 2.13, 2.14). It is also intended that it should be possible to remove the whole apparatus from the beam line as one unit.

The experimental hall will need to be excavated to a depth of approximately 4m below beam height over an area of 12m (along the beam) x 20m (perpendicular to the beam). The excavation should be asymmetric relative to the beam line. On one side we require sufficient space to remove the apparatus completely from the beam and remove sections A and C away from each side of the inner detector. (We estimate we need 13m of floor space for this). On the other side of the beam pipe we would wish to be able to remove sections A and C leaving the inner detector in situ. For this we require 7m of floor space.

2.7 The Two Photon Tagging System

We require a positive identification of electron/positron tracks coming at angles between 30 and 80mr from the interaction point, and a

measurement of energy sufficiently accurate to identify unambiguously Bhabha scatters and to give an estimate of the centre of mass energy W. The situation will be complicated by very low energy electrons and photons produced by the synchrotron radiation and by Bremsstrahlung electrons and photons. Even though the beam pipe and machine optics have been designed to minimize these backgrounds, and the beam pipe is surrounded by 2cm of lead, the apparatus is designed to function in the presence of large "singles" rates in the counter elements, and the angular resolution is sufficient to reject tracks originating away from the interaction point.

In fig. 2.15 we show the layout of the tagging system on one side of the interaction point. Charged particle tracks are identified by a set of drift chambers placed normal to the beam direction and close to the pipe. Each chamber is divided into 5cm modules by alternating high voltage and signal wires. The electronic readout is arranged so that there is a 3mm radial resolution and "4 hit" capability within each module. Adjacent chambers are built with an alternating pattern of detector modules to resolve the left-right ambiguity (fig. 2.16). There are two sets of chambers placed about 1m apart so that the angular resolution $\Delta\theta$ of tracks is better than 3mr. This resolution ensures that from a coincidence of two tracks, one in each tagging system, we can reconstruct the common interaction point to better than 1m in the beam direction and better than 2cm normal to the beam. Beam-gas Bremsstrahlung tracks emanating from the collimators at the ends of the experimental area will thus be effectively rejected. We estimate also that the system will identify unambiguously a track provided that the average number of single "sparks" in each chamber

is less than 3.

The design and method of construction of the chambers follows closely the example of the drift chambers built at the Daresbury Laboratory for the E.M.C. at CERN. Each chamber has an active area of 30cm x 80cm with 10mm gap between 15mm sheets of "Rohacell" rigid foam. The field shaping electrodes are etched onto printed circuit board bonded to the "Rohacell" sheets. In figs. 2.16 and 2.17 we show a schematic of the chamber construction.

Positive identification of electrons and positrons is simply and conveniently achieved by a 15 radiation length wall of lead-glass bricks (8cm x 8cm x 40cm), fig. 2.18. The theoretical energy resolution of such a system is $\pm 6/E^{1/2}\%$. This is sufficient to effectively reject low energy (< 500 MeV) Bremsstrahlung photons. At the other extreme of the energy range the resolution is good enough to separate elastic scattering events (E_1, $E_2 \approx E$). There are two more reasons for implementing a cut on E_1 and E_2 at high energy . One is the fact that the energy resolution $\frac{\delta W_{\gamma\gamma}}{W_{\gamma\gamma}} \simeq \frac{1}{2} \frac{\delta E_1}{(E-E_1)}$ $(E_1 \gg E_2)$ diverges as $E_1 \to E$, the other is that the centre of mass to laboratory transformation factor $\gamma\beta$ also diverges as $E_1 \to E$ leading to large distortions of the hadron angular distributions.

The total amount of material traversed by an electron between the interaction point and the lead glass array is equivalent to 0.03 radiation lengths. The effect of this on the angular and energy resolution of electrons will be less than the intrinsic resolution of the drift chambers and lead glass.

Both the chamber package and lead glass array are designed to split symmetrically and can be withdrawn from around the beam pipe. The assemblies can then be craned away leaving working space when the central detector

end caps are removed.

In the following table we summarise the main parameters of the tagging system

Aperture	$30mr < \Theta_1, \Theta_2 < 80$ mr
Angular resolution	$\Delta\theta \lesssim 3$mr
Energy range	1 GeV $\lesssim E_1, E_2 \lesssim E$
Energy resolution	$\Delta E_{1,2} \approx \pm 6/E_{1,2}^{1/2}\%$
Chamber active area	30cm x 80cm
Number of chambers	16 on each side of I.P.
Number of readout channels	96 on each side of I.P.
Number of leadglass blocks	92 on each side of I.P.
Total thickness of chambers	$\lesssim$ 0.03 radiation lengths

2.8 Compensating Solenoid

The central detector magnet and compensating solenoid have to fulfil the following requirements:

a) $\int_0^L \bar{B}\, dl = 0$ where 2L is the distance between the tungsten collimators

b) $\Delta\nu \leq 0.02$ for each compensating solenoid (11)

The tune shift $\Delta\nu$ is given by the expression (12):

$\Delta\nu = (1.79 \times 10^{-3}/p^2) \int B^2 \beta(1) dl$

where $\beta(1)$ is the betatron function and is determined by the magnetic configuration of the ring. In our case the vertical function $\beta_y(1)$

dominates and in the straight sections is given by

$$\beta_y(1) = \beta_y(o) + 1^2/\beta_y(o) \ ;$$

Assuming $\beta_y(o) = 0.3$ m (13) for the 15m long interaction region at Petra, we can write after some manipulation:

$$\frac{\Delta\nu\, p^2}{B_s^2} = 5.97\times10^{-3}\, l_s^3 \left(\frac{1}{3} + \frac{l_c}{3l_s} + \frac{L(L - l_c)}{l_c\, l_s} \right) \ ;$$

where B_s is the central solenoid field in Tesla,

p the beam momentum in GeV,

l_c the length of one compensator coil in m

$2\, l_s$ the length of the central solenoid in m.

Using $B_s = 0.5$ Tesla, $l_s = 1.75$m, $L = 7.0$m and $\Delta\nu \leq 0.02$ we require $l_c \geq 0.45$m when the beam energy is 5 GeV. There may be adverse effects on the stored beam due to higher order fields at the entrance and exit faces of the 22cm diameter compensator. We feel it desirable to increase the length to 0.85m which then implies a compensator field $B_c = 1$ Tesla, and a power requirement of 120 kW for each magnet. The location of the compensators is illustrated in fig.2.1.

2.9 Luminosity Monitor

The proposed tagging system is well suited for use as a luminosity monitor at our interaction point by measuring Bhabha scattering at small angles. In the angular range $30 \leq \theta \leq 80$ mrad, corresponding to momentum transfers squared $q^2 < 1$ GeV^2, Q.E.D. has been proven to hold. A highly symmetrical arrangement of counters is essential in order to be insensitive to transverse displacements of the beams. Also the aperture of these counters has to be carefully chosen in order to keep the

radiative corrections small and to be insensitive to small longitudinal interaction point displacements.

The counting rate in this monitor at E = 15 GeV and $L = 5 \times 10^{30}$ cm^{-2} sec^{-1} will be about 5/sec. Similar systems are already in use as luminosity monitors and accuracies up to 1% have been achieved(14).

Peferences

1) DESY Heidelberg Group, presented by J. Heintze, Discussion Meeting on Petra Experiments, Frascati (1976), page G60

2) G. Charpak et al., Nucl. Instr. and Meth. 108 (1973) 431

3) W.W.M. Allison et al., Nucl. Instr. and Meth. 133 (1976) 325

4) Aderholz et al., Nucl. Instr. and Meth. 118 (1974) 419

5) Cobb et al., Nucl. Instr. and Meth. 133 (1976) 315

6) F. Dyclak et al., submitted to Nucl. Instr. and Meth., May 1976 and P. Steffen, private communication

7) M. Holder et al., Nucl. Instr. and Meth. 108 (1973) 541
J.S. Beale et al., Nucl. Instr. and Meth. 117 (1974) 501
J.A. Appel et al., Nucl. Instr. and Meth. 127 (1975) 495
Ch. Berger et al., Nucl. Instr. and Meth. 130 (1975) 507

8) A. Carrol et al., PEP Summer Study Report (1975) 176

9) J. Engler et al., Nucl. Instr. and Meth. 106 (1973) 189

10) F.A. Harris et al., Nucl. Instr. and Meth. 103 (1972) 345

11) G. Voss, private comm.

12) W.A. Wenzel, PEP-note no. 127, Feb. 1976

13) K. Steffen, private comm.

14) B.L. Beron et al., submitted to Phys. Rev. Lett. and L. O'Neill, private comm.

Figure Captions

Fig. 2.1 The beam pipe

Fig. 2.2 Configuration of the coil windings

Fig. 2.3 Principle of a jet chamber. The chamber is indicated in both views in the lower part of the figure. The numbers 1 - 4 refer to particle tracks. The open circles represent potential wires providing the driftfield. Σ is an adding circuit, D a discriminator.

Fig. 2.4 Internal detector, radial section

Fig. 2.5 Internal detector, transverse section

Fig. 2.6 Detail of chamber 3 (Scale 1:1); for explanations see text

Fig. 2.7 Spatial resolution vs driftpath x for various gases
a) 75% Propane + 25% Ethylene at 4 Atm.
b) the same gas at 1 Atm
c) 2/3 Argon + 1/3 Isobutane at 1 Atm.

Fig. 2.8 Amplitude recorded at both ends of a counter (2.5m long, anode wire 20μ Ø tungsten) with radiation incident at different distances Z from the middle of the counter.

Fig. 2.8a Two dimensional display of the amplitudes shown in Fig. 2.8 a) expected distribution for ideal resolution, b) experimental results

Fig. 2.9 Magnetic deflection (Sagitta S_M), multiple scattering (rms Sagitta σ_{sc}) and spatial resolution σ_ϕ (high precision readout) as a function of momentum p.

Fig. 2.10 Arrangement and support of leadglass blocks surrounding the coil

Fig. 2.11 Leadglass energy resolution as a function of energy for various thicknesses of Al in front of the counter

Figs. 2.12, 2.13, 2.14 The muon filter

Fig. 2.15 Schematic layout of one half of the tagging system. Distances are from interaction point.

Fig. 2.16 Schematic detail of ambiguity resolving double drift chamber

Fig. 2.17 Arrangement of drift chambers in front of leadglass detector

Fig. 2.18 Elevation of one half of symmetric leadglass detector

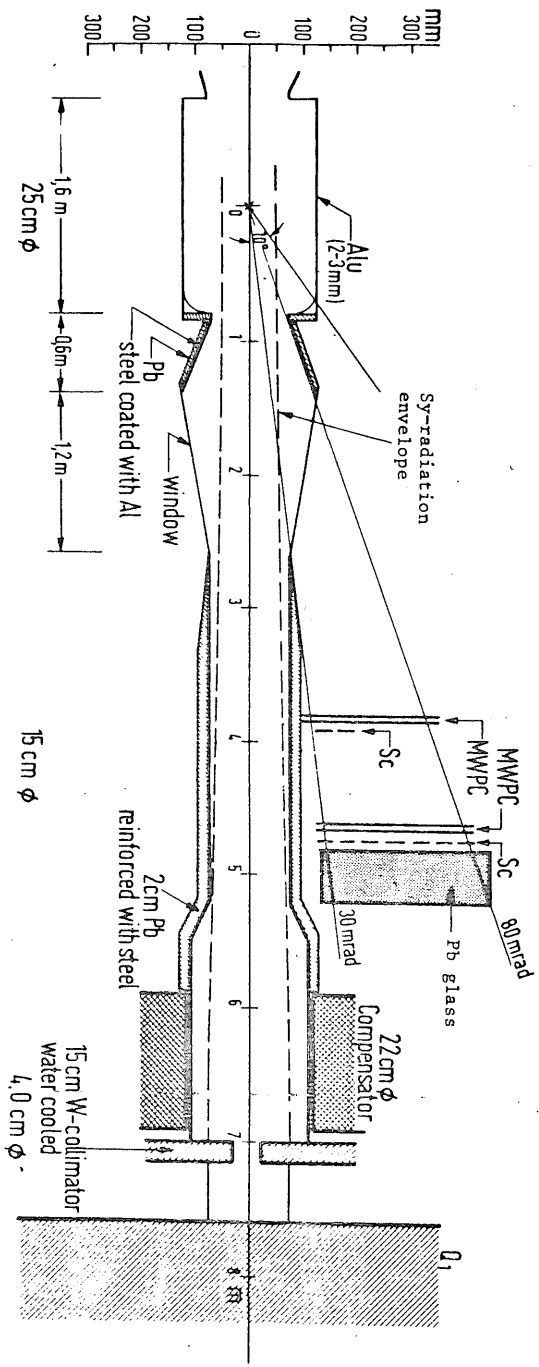

Fig. 2.1

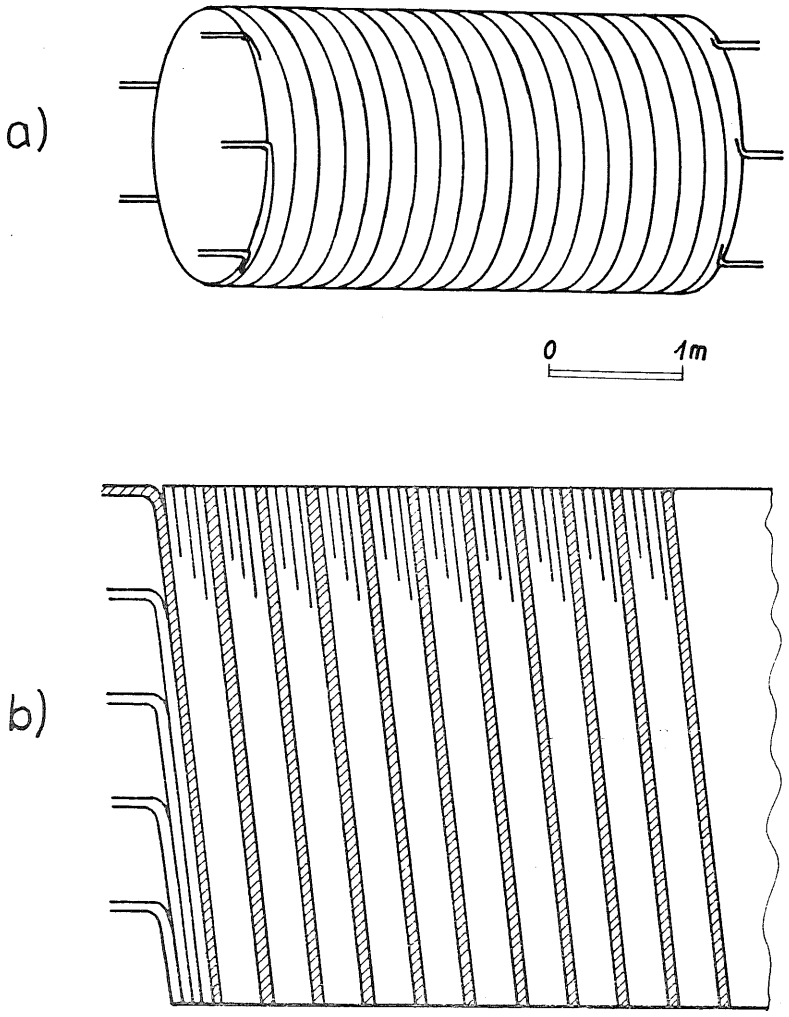

Fig. 2.2

a) General view (to scale) of one layer of the coil showing the position of the five water and electrical connections at each end.

b) Schematic view of the winding arrangement of one layer. One of the water circuits is shown shaded for clarity.

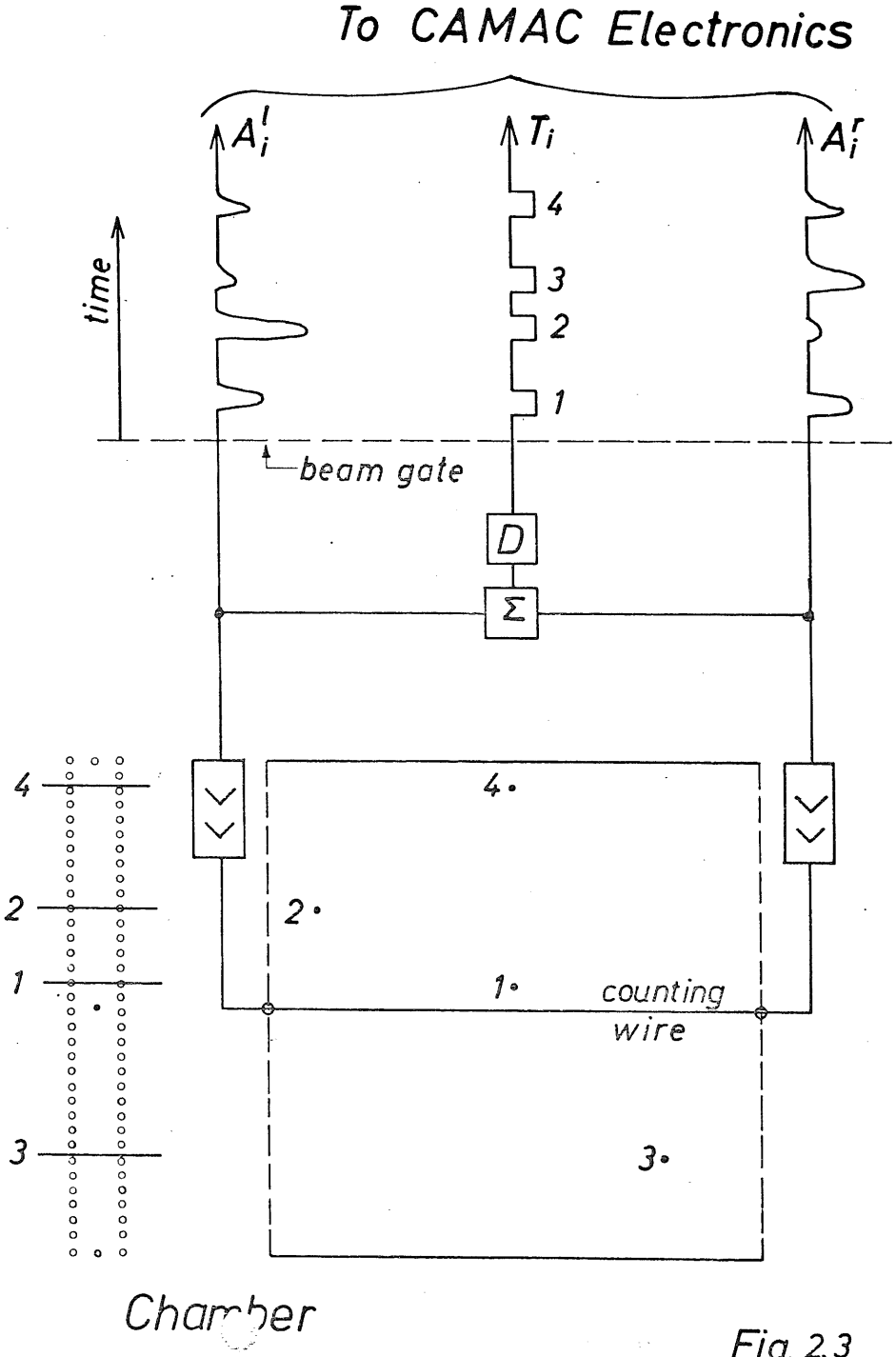

Fig. 2.3

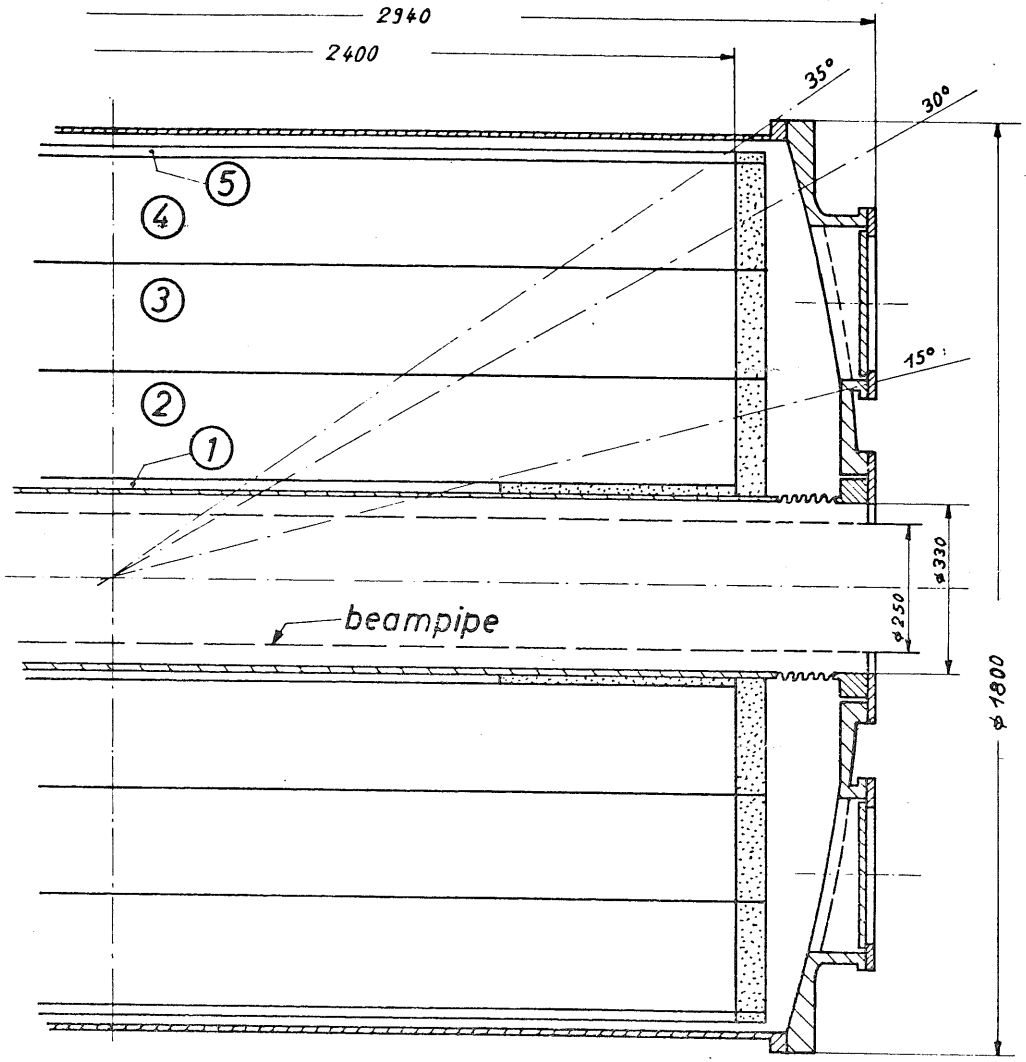

Fig. 2.4

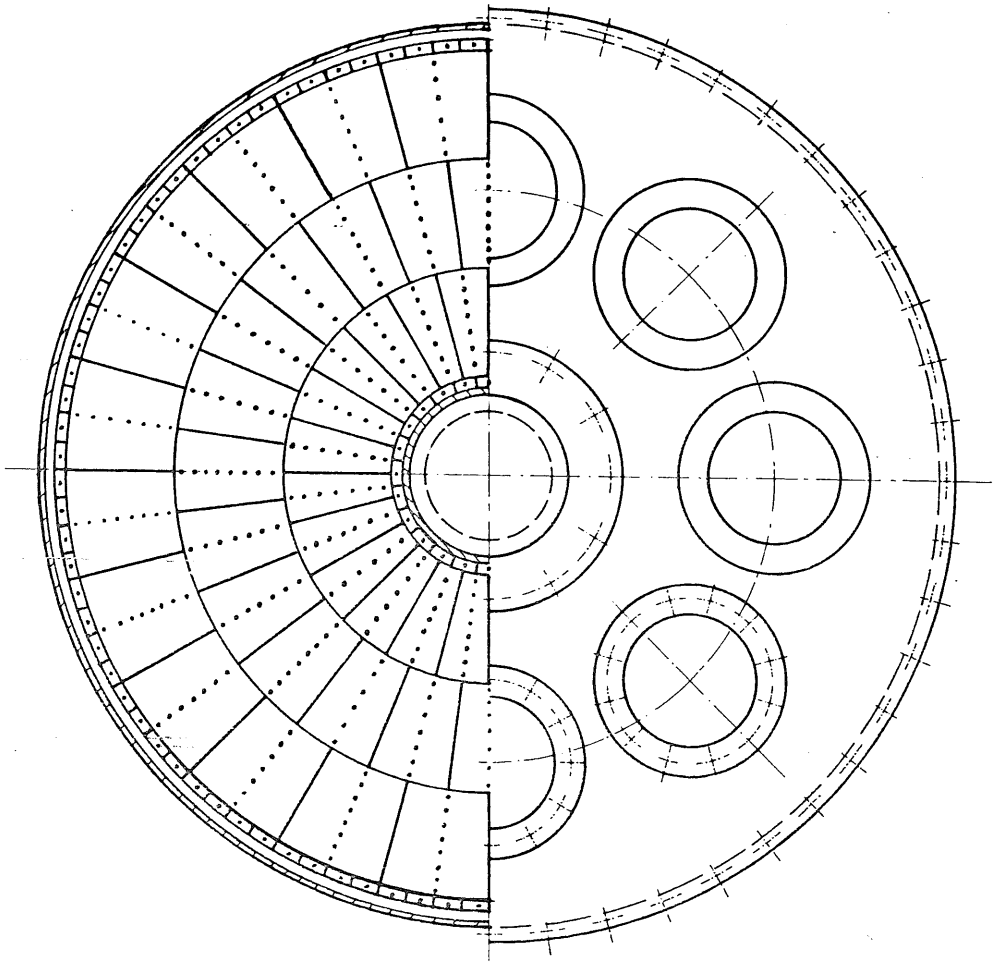

Fig. 2.5

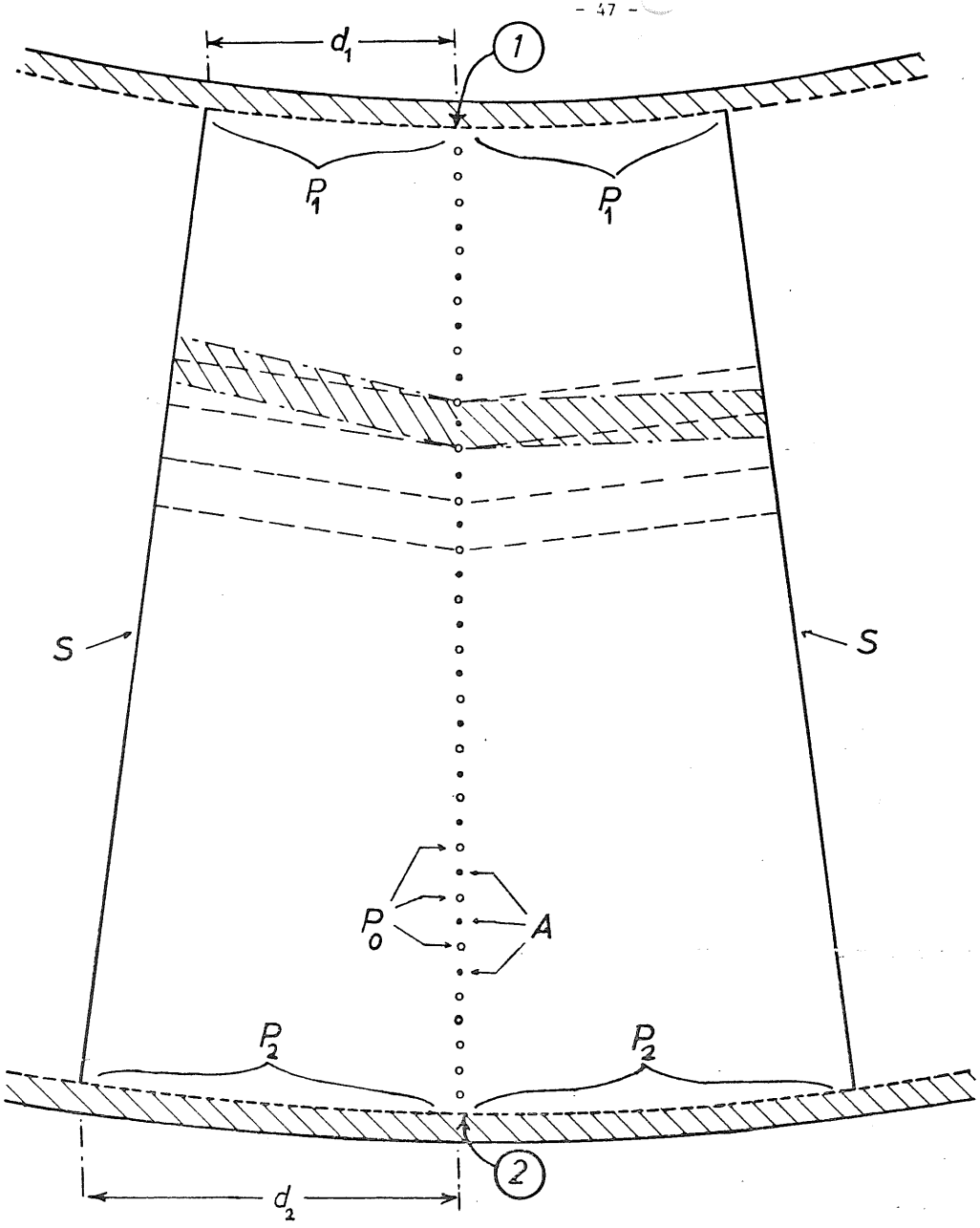

Fig. 2.6

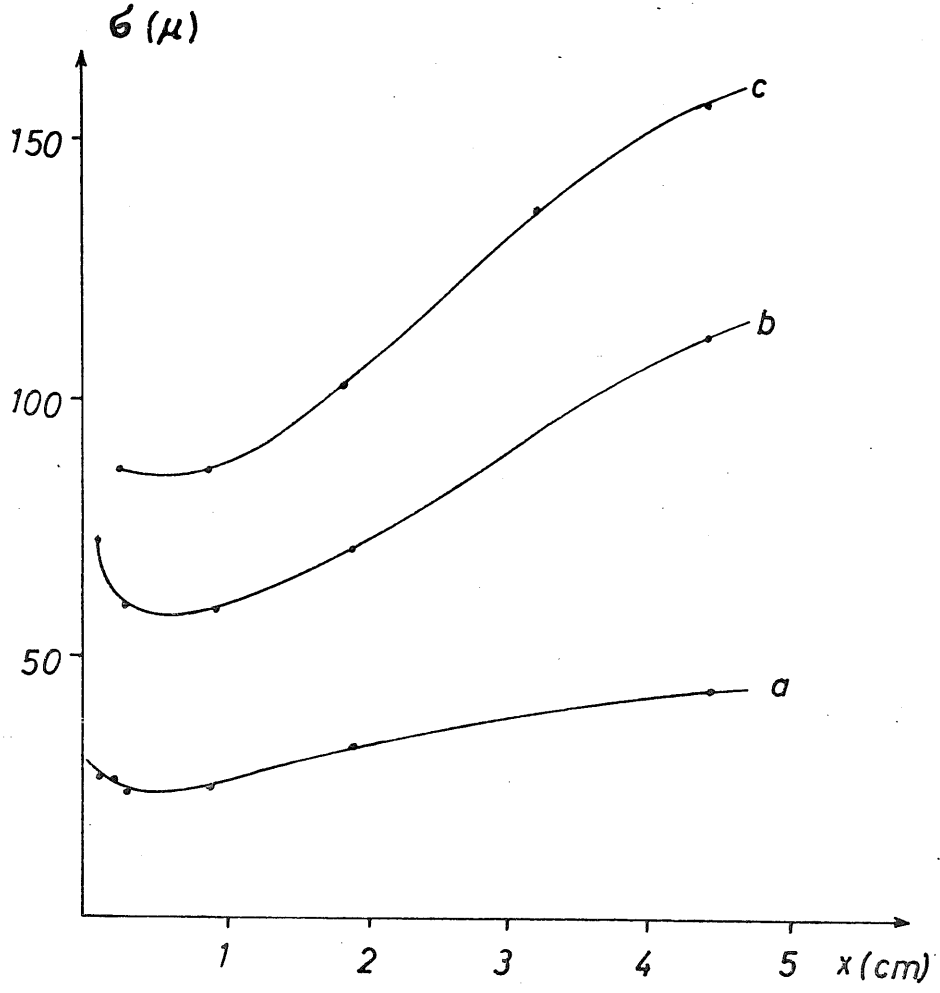

Fig. 2.7

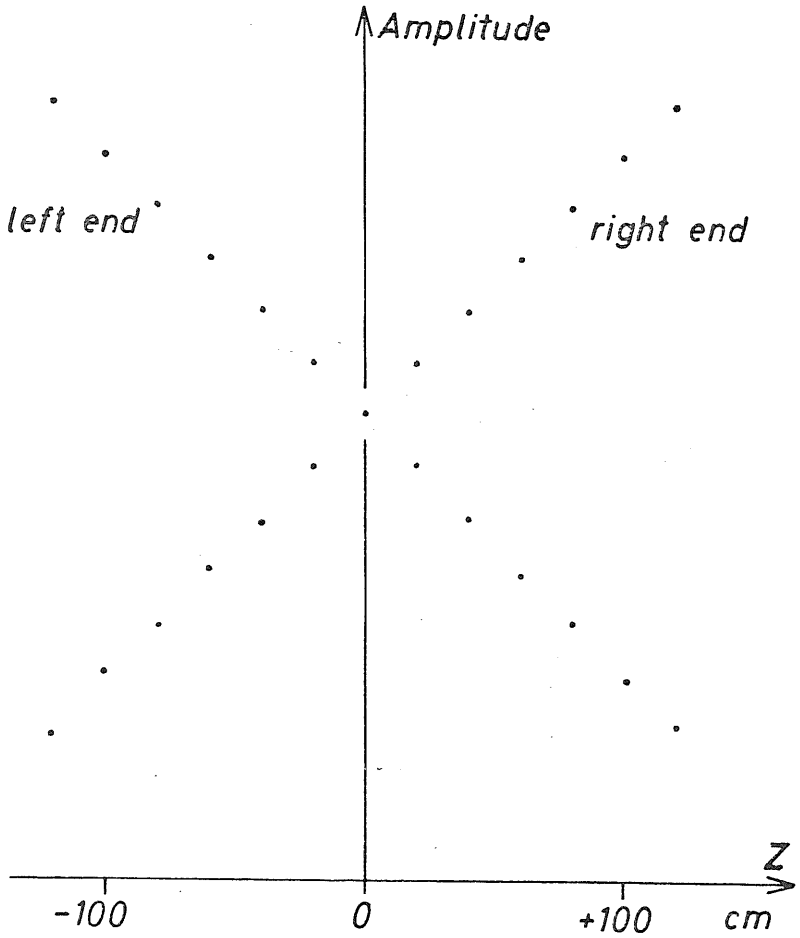

Fig. 2.8

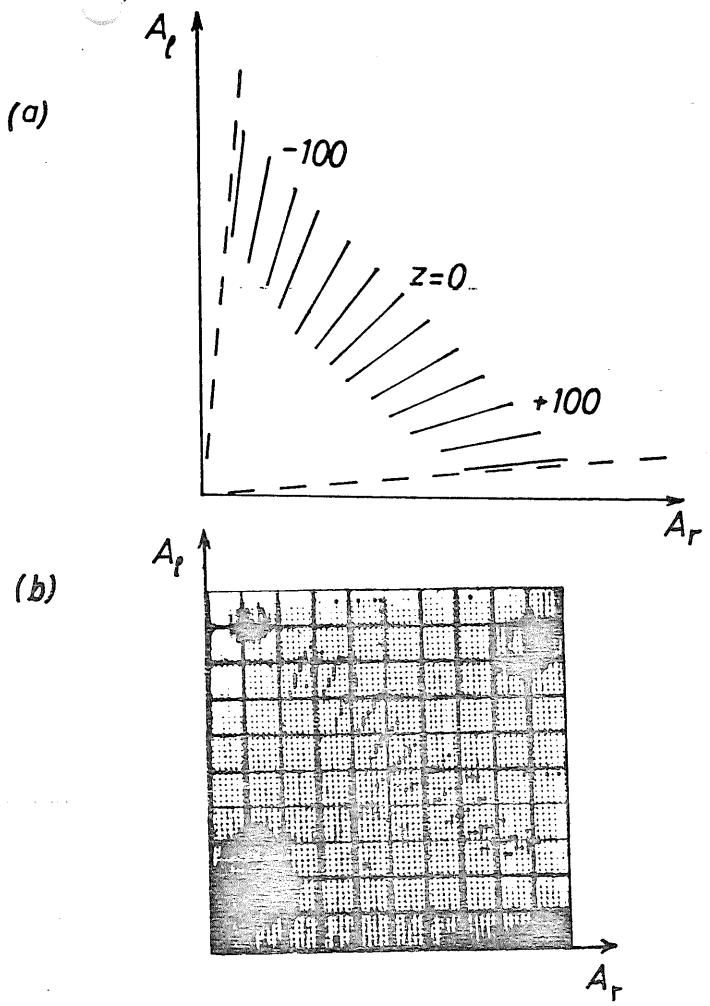

Fig. 2.8a

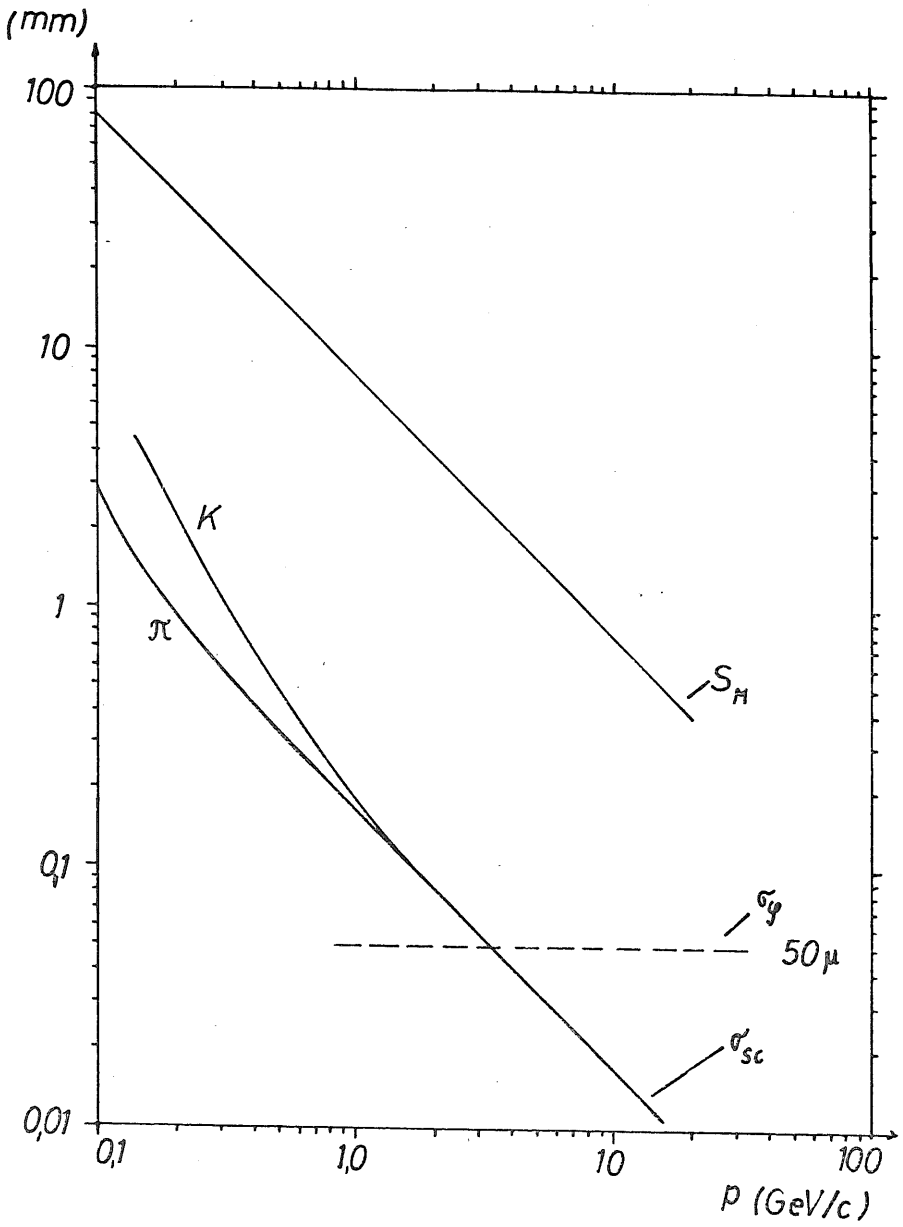

Fig. 2.9

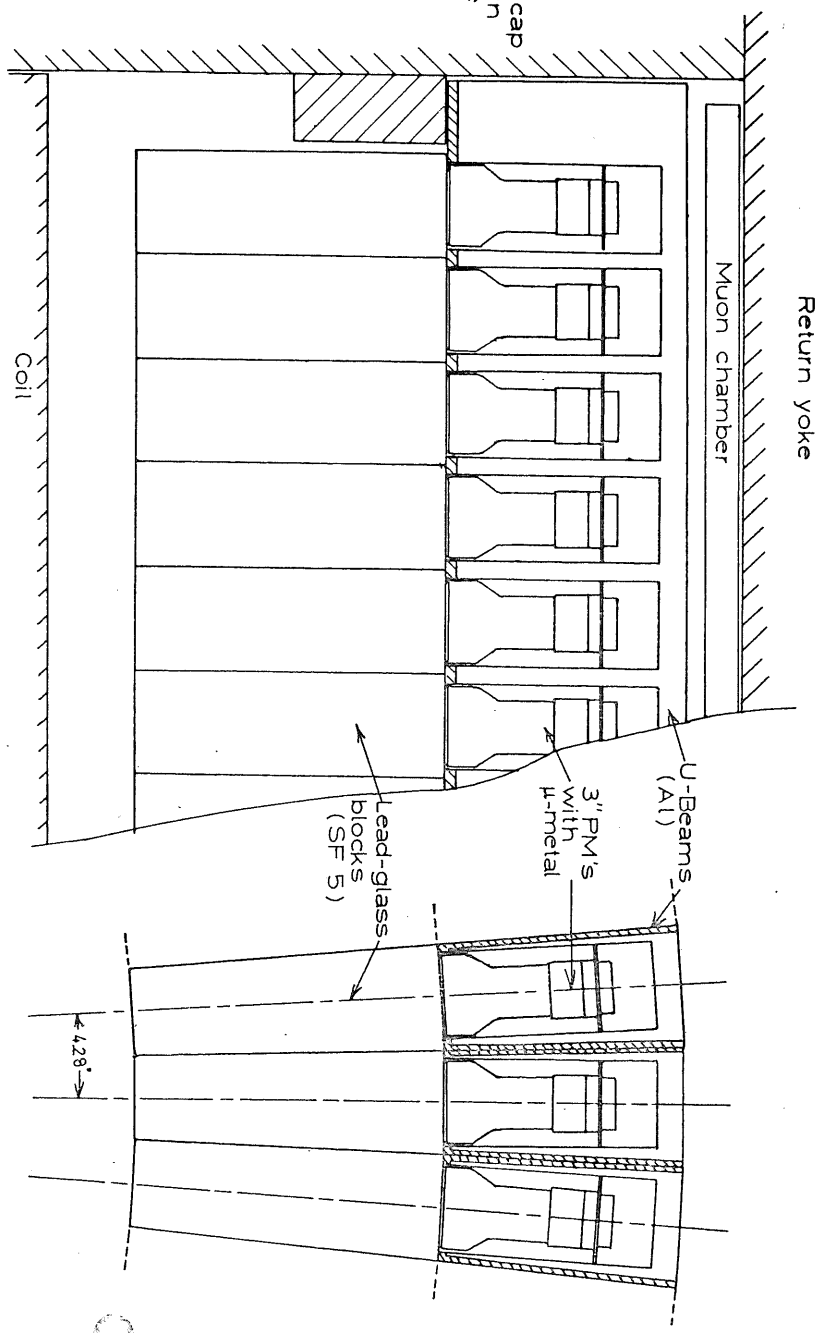

Fig. 2.10

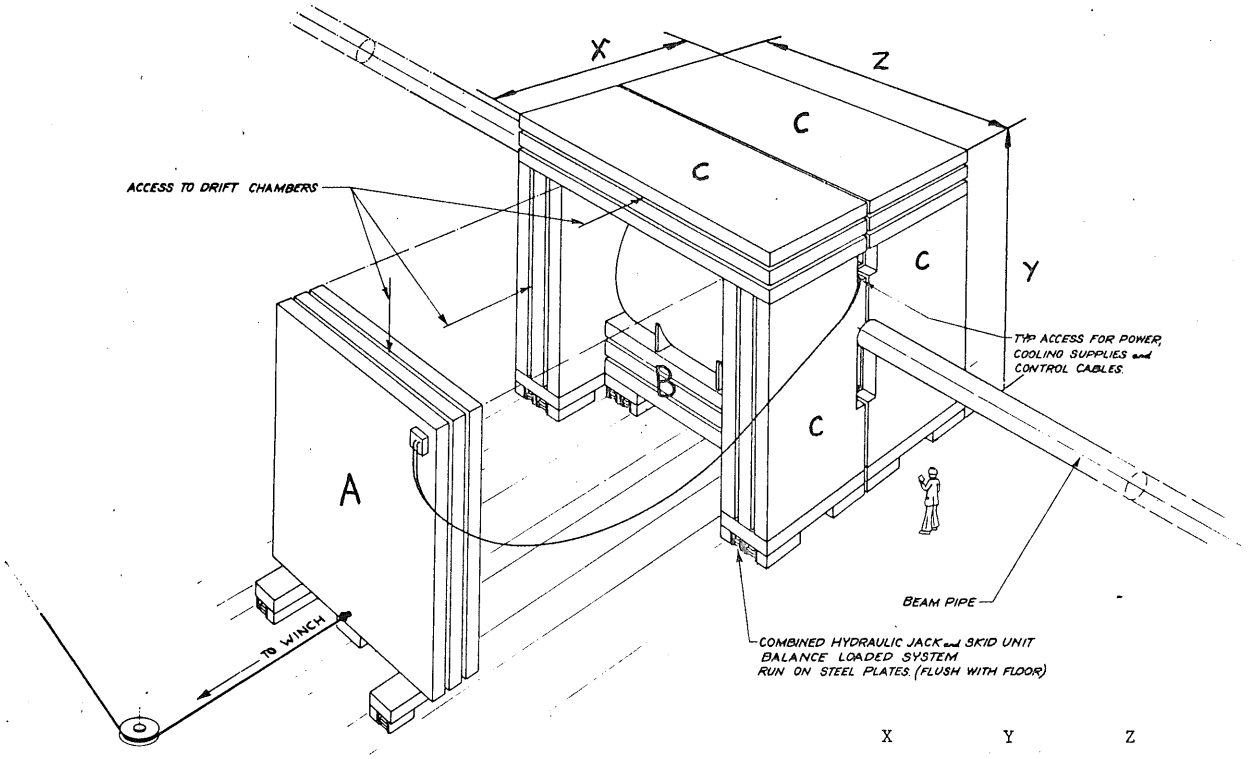

	X	Y	Z
Steel Version	5.6 m	6.05 m	6.95 m
Concrete Version	6.45 m	6.76 m	7.75 m

Fig. 2.12

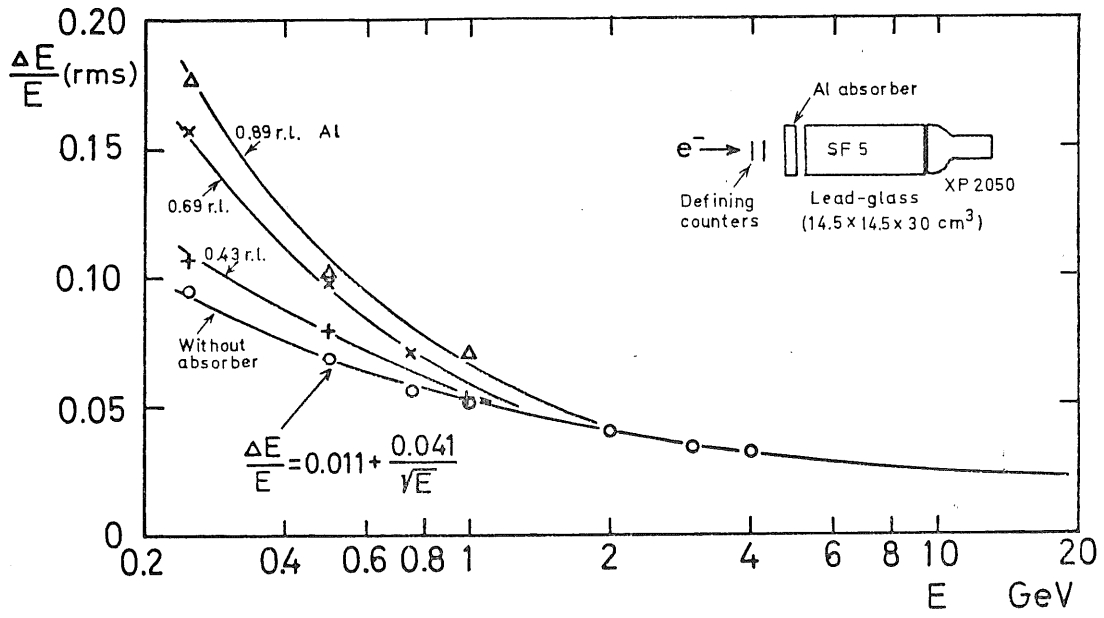

Fig. 2.11

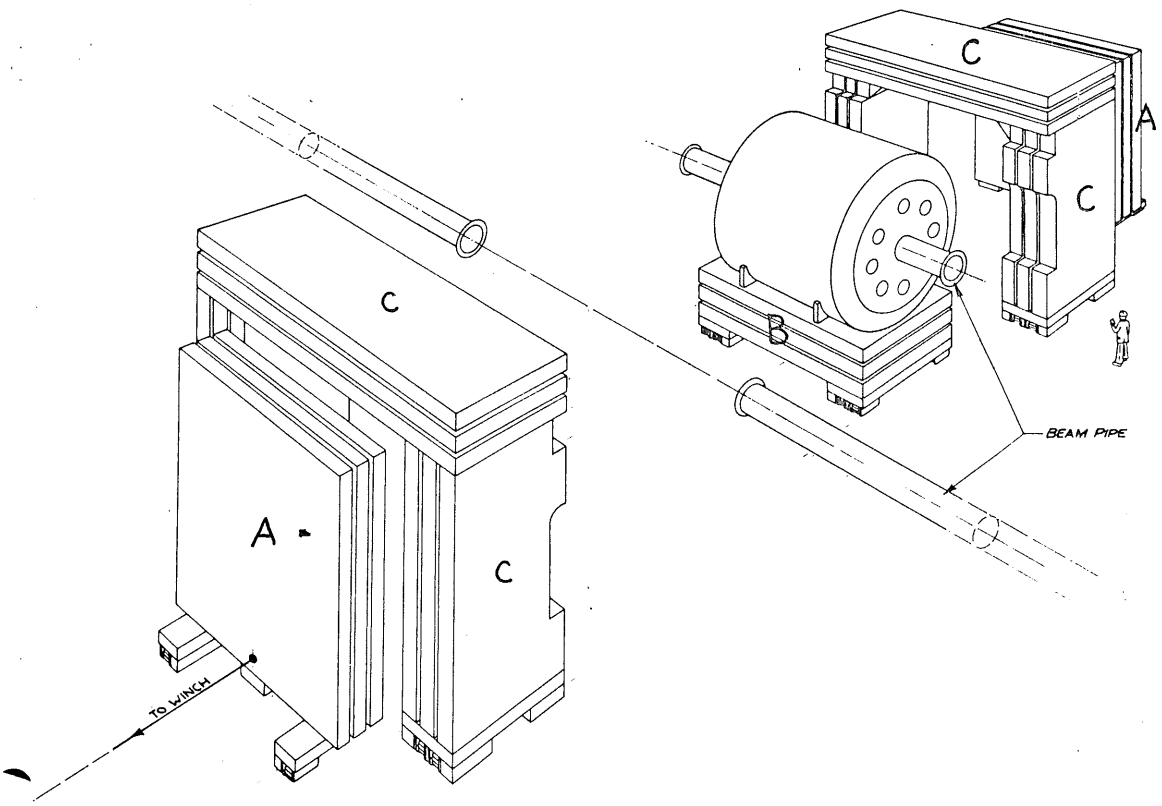

Fig. 2.14

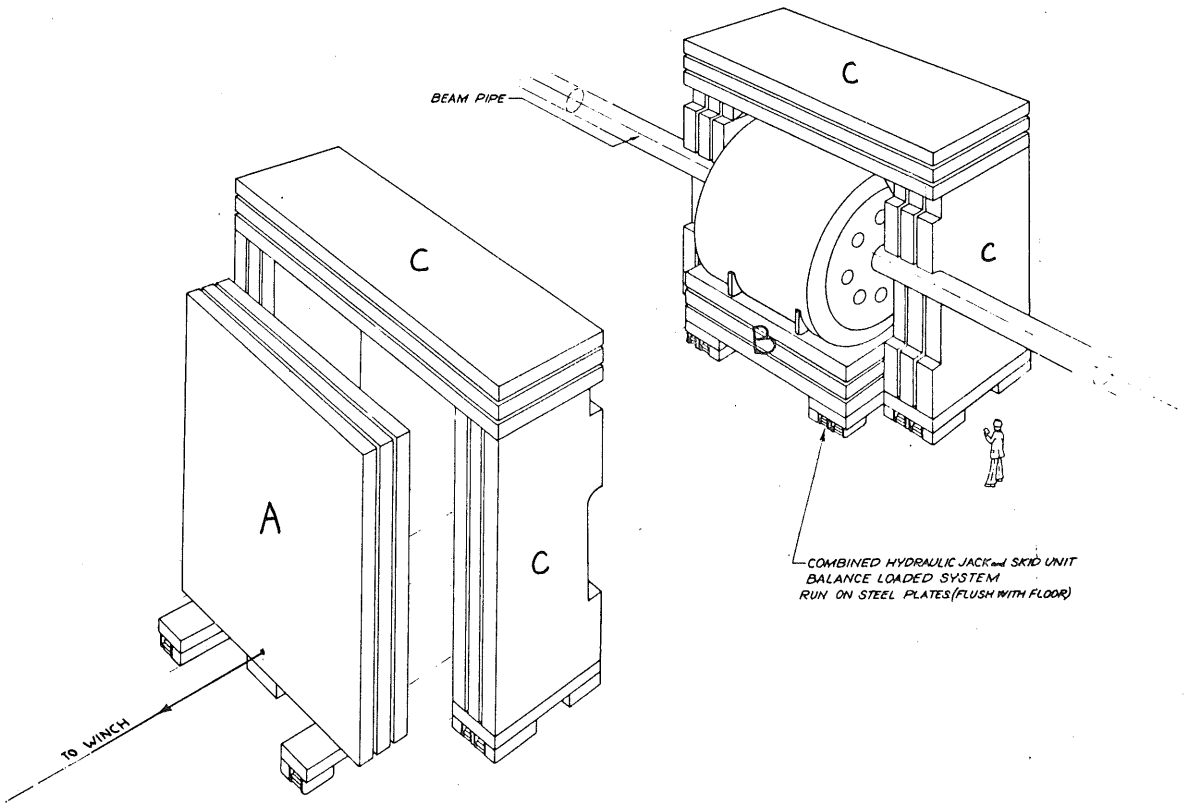

Fig. 2.13

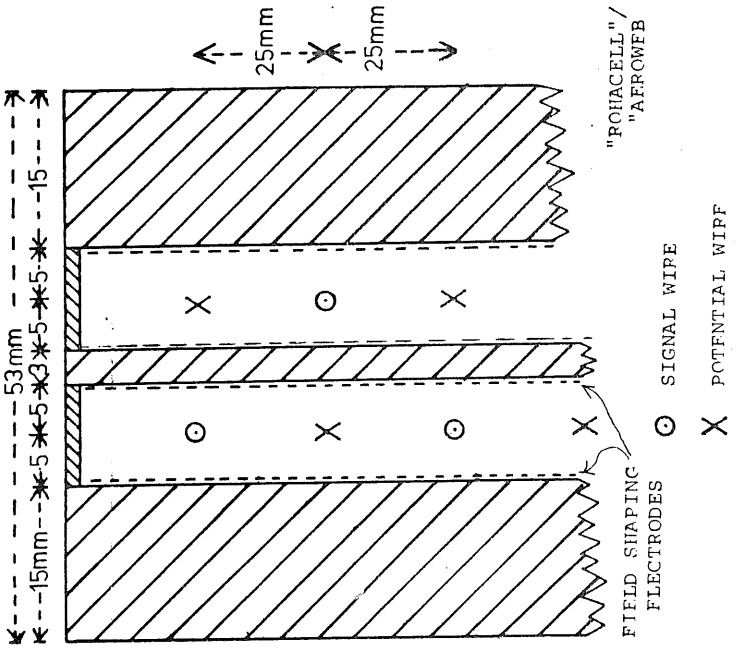

SCHEMATIC DETAIL OF AMBIGUITY RESOLVING
DOUBLE DRIFT CHAMBER

Fig. 2.16

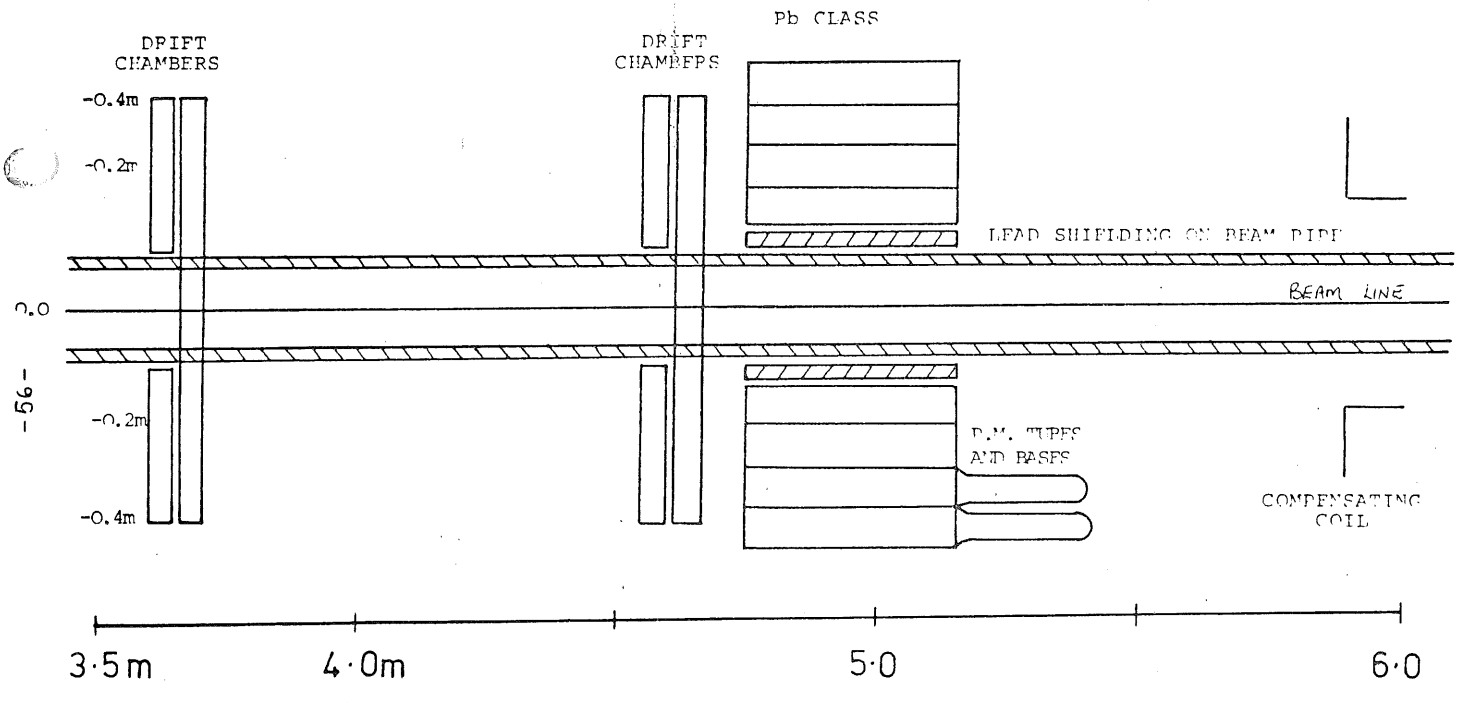

SCHEMATIC LAYOUT OF TAGGING SYSTEM

Fig. 2.15

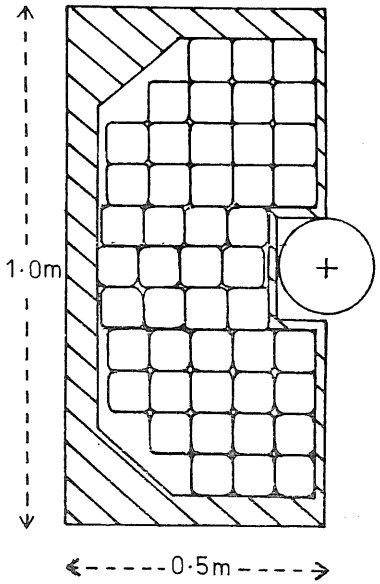

ELEVATION OF ONE
HALF OF SYMMETRIC
Pb GLASS DETECTOR

Fig. 2.18

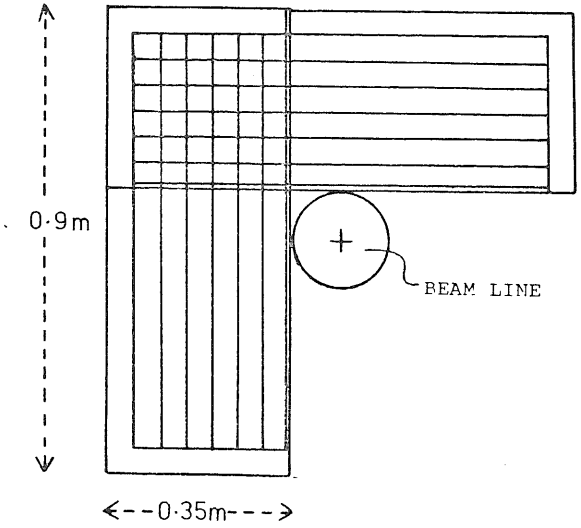

ARRANGEMENT OF 2 OF 4 DRIFT CHAMBERS
LOCATED IN FRONT OF Pb GLASS DETECTOR

Fig. 2.17

3 TRIGGER, DATA ACQUISITION AND COMPUTING REQUIREMENTS

The proposed detector with two layers of scintillation counters 75cm apart, lead glass shower counters and fast track finding logic (described in the appendix) provides a powerful and flexible trigger. The trigger system on the one hand must not introduce a significant bias against beam-beam events and on the other hand should give a sufficient rejection of background events to make the data acquisition and data analysis feasible. Experience shows that the details of the trigger mode can only be decided in the testing phase of the experiment. In the following we therefore present only a trigger scheme and show, making realistic assumptions that the apparatus is powerful enough to handle the expected background rates and that the data acquisition and data processing is feasible.

3.1 The Trigger Scheme

The trigger scheme is sketched in fig. 3.1. A matrix coincidence between the trigger counters and the time-of-flight counters defines a charged particle track. The minimum transverse momentum cut-off due to this coincidence is 80 MeV/c. It can however be increased, if necessary. For the end cap part of the detector lead glass counter signals are used instead of time-of-flight counter signals since this region is not covered by time-of-flight counters. If it turns out that the twofold coincidences are insufficient, we can further demand a coincidence with the signals from the lead glass counters. The "charged" track signals are used together with signals from the lead glass counters, the track finding logic, the μ-chambers and the tagging

counters to form the various event triggers indicated in fig. 3.1. A "neutrals" trigger signal is formed if the energy deposited in the lead glass exceeds a certain threshold. For the trigger "n prongs + neutrals" this threshold decreases with increasing prong number. Such a trigger bas been successfully used by the DESY-Heidelberg collaboration at DORIS.

3.2 Estimated Background Rates

We consider only background effects which may simulate genuine beam-beam events. Synchrotron radiation, which is not of this kind, is discussed in sec. 2.1.

The signal rate from cosmic rays will be about 1.6 kHz in the time-of-flight counters and 80 Hz in the trigger counters. Demanding a coincidence between the trigger and the time-of-flight counters will yield a background rate of 80 Hz provided the single rates in these counters are sufficiently low to neglect random coincidences. This rate can be further reduced by the factor $\frac{\text{gate width}}{\text{repetition time}} = \frac{20 \text{ nsec}}{2 \mu \text{ sec}} = \frac{1}{100}$ since we gate our electronics with the beam signal. This trigger rate of about 1 Hz can be further reduced by about one order of magnitude with the help of the track-finding logic. In the final analysis, this background is easily separated from a beam-beam event by the complete track analysis and by the time-of-flight information.

Another important source of background is beam-gas interactions close to the beam-beam interaction region. Assuming a vacuum of 2×10^{-9} torr in the interaction region, we estimate a background rate of about 1/sec/m

from events in which hadrons are produced. Most of these events show a simple pattern (only the recoil nucleon entering the detector), and one might hope to eliminate them in the trigger without introducing a significant bias against beam-beam-interaction events. Further reduction of this rate is achieved at the track finding stage.

The proposed detector is quite insensitive to background from "beam-halo" particles since the time-of-flight counters and the lead-glass counters can be effectively shielded against these particles. In addition the track finding logic provides further rejection. The actual rate of this background is difficult to estimate since it depends critically on the machine parameters (position of scrapers etc.) and on the shielding.

3.3 Data Acquisition

Data are collected from approximately 3000 drift wires and 4000 photo tubes. To estimate the amount of information to be processed, we recall that the maximum number of signals per drift wire is 8 for the inner detector and 4 for the μ-filter, and each track signal produces 1 TDC and 2 ADC values per wire, i.e. 3 words/wire (here and in the following, 1 word = 16 bits). Since the analog to digital conversion is a slow process it is done in parallel for all the wires, and the digital values are stored in a CAMAC memory with a capacity of 25 words per wire for the inner detector and 13 for the μ-filter. Altogether there are about 50 000 such memory locations (scattered over 35 crates) containing the relevant information. This clearly shows the need for a fast data scanner which is able to skip empty memory locations

within 100 to 200 nsec, and to read the condensed track information into the on-line computer in not more than 10 to 20 msec. A second such scanner is projected for reading the phototube information. These scanners are linked via data channels 1 and 2 to the on-line computer as shown in fig. 3.2.

In addition to the fast data channels a conventional CAMAC branch is needed which has a lower transfer rate but provides all the CAMAC functions, thereby serving as a general purpose data path. In particular, alarm interrupts and transfer of control and status information can proceed via this third channel which has to be equipped with interrupt vectors to allow for quick program response. Scalers, power control units and the pattern of the event trigger and of the track finding logic are connected to the CAMAC branch in order to provide greater flexibility in selecting or adding information needed for the data analysis. For operating the scalers independently of the computer and for testing the various CAMAC functions, the respective scanning and display units are inserted into this branch. All three data paths, presented in fig. 3.2, are equipped with direct memory access into the computer and programmed transfers in both directions. This allows computer controlled testing of the data paths.

The on-line computer accumulates the data and performs consistency checks before sending the data to the IBM 370/168 for storage on magnetic tape. Also it is necessary to monitor the functioning of the many detector components and, on operator command, to request feedback information from the analysis program in the IBM 370/168. The demand on the on-line computer will be especially high at times of final checkout before and during the data taking period. In order to allow different components to

be tested and programs to be developed at the same time the operating system of the on-line computer has to provide multi-job processing. This necessitates a large core storage. As indicated in fig. 3.2 a fast storage capacity of 192 Kwords (16 bits each) and two disks of 4 Mwords each for program libraries are assumed. Further peripheral devices are 3 terminals and 3 displays as well as backup tapes or floppy disks for programs, a card reader, a hard copy unit and a line printer.

The total cost estimate for all components is given in sec. 5.2. The costs for the data paths connected to channels 1 and 2 only include the crate controllers and the connecting cables. The additional expense for crates is contained in the estimates for the wire chamber and photo-tube electronics. For the general purpose CAMAC branch, however, the price for the crates is also added into the amount given.

3.4 Date Reduction

Given this approach, it is of great advantage to use the flexibility of a large computer system and implement later any system of hardware aided event analysis. The most economic use of computer power is obtained if the event analysis for feedback or monitoring purposes and for data reduction are done in a single step, since the unpacking and the attempted reconstruction of the event has only to be done once. These arguments favour a powerful on-line program at the IBM 370/168.

An on-line program at the IBM needs 128 Kwords (16 bits each) virtual fast storage and a disk space of 50 Mwords. The transfer line between the on-line computer and the IBM should allow a peak rate of 10 Kwords/sec although the transfer rate depends on the event trigger and the average

event length. Because of the dense packing of the drift chambers in the inner detector a single track produces roughly 250 words and a clean cosmic ray background event has of the order of 500 words. For a mean track number of 4 - assuming the presence of noise and averaging low multiplicity background and real high multiplicity hadronic interactions - one obtains an average event length of about 1000 words. If the trigger rate is about 1 per second, the transfer rate to the IBM is not very much higher than for present storage ring experiments.

3.5 Computing Requirements

Experiments at PETRA will obviously have to be analysed in parallel with the data taking. Therefore, an efficient data analysis can be done only if sufficient computing time is available on site.

As an estimate of the computing time needed we take the order of magnitude of present storage ring experiments plus an additional 20 to 30%, to account for a more complex detector.

for on-line analysis and data reduction	10%	(% of IBM 370/168
for event reconstruction and final analysis	30%	CPU time)
and a total of	40%	

It is conceivable that for the off-line analysis the equivalent of 10% IBM 370/168 time can be obtained from the Rutherford Laboratory which would reduce the above number to 30% CPU time (corresponding to about 15% of the computer capacity presently available at DESY). However, a necessary prerequisite would be the establishment of a data

link between the two laboratories for the transfer of programs and analysed data, and the establishment of a work station for the Rutherford computer at DESY. The actual load on the Rutherford computer is expected to be 20% equivalent IBM 370/168 time, since the transfer of part of the data analysis to another computer will necessarily create some overlap. The problems of format standardization and conversion are presently under investigation.

Figure Captions

Fig. 3.1 Trigger scheme

Fig. 3.2 Data flows from the detector to magnetic tape

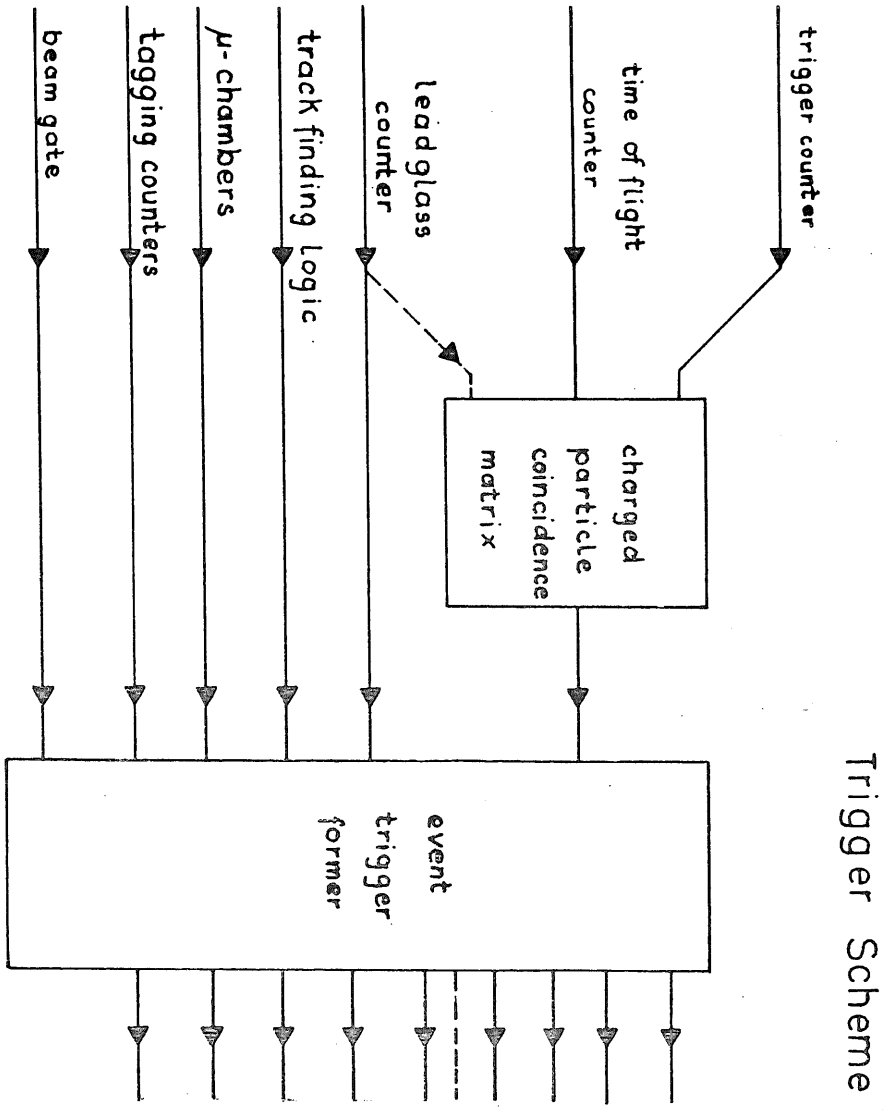

Fig. 3.1

Data Flow from the Detector to Magnetic tape

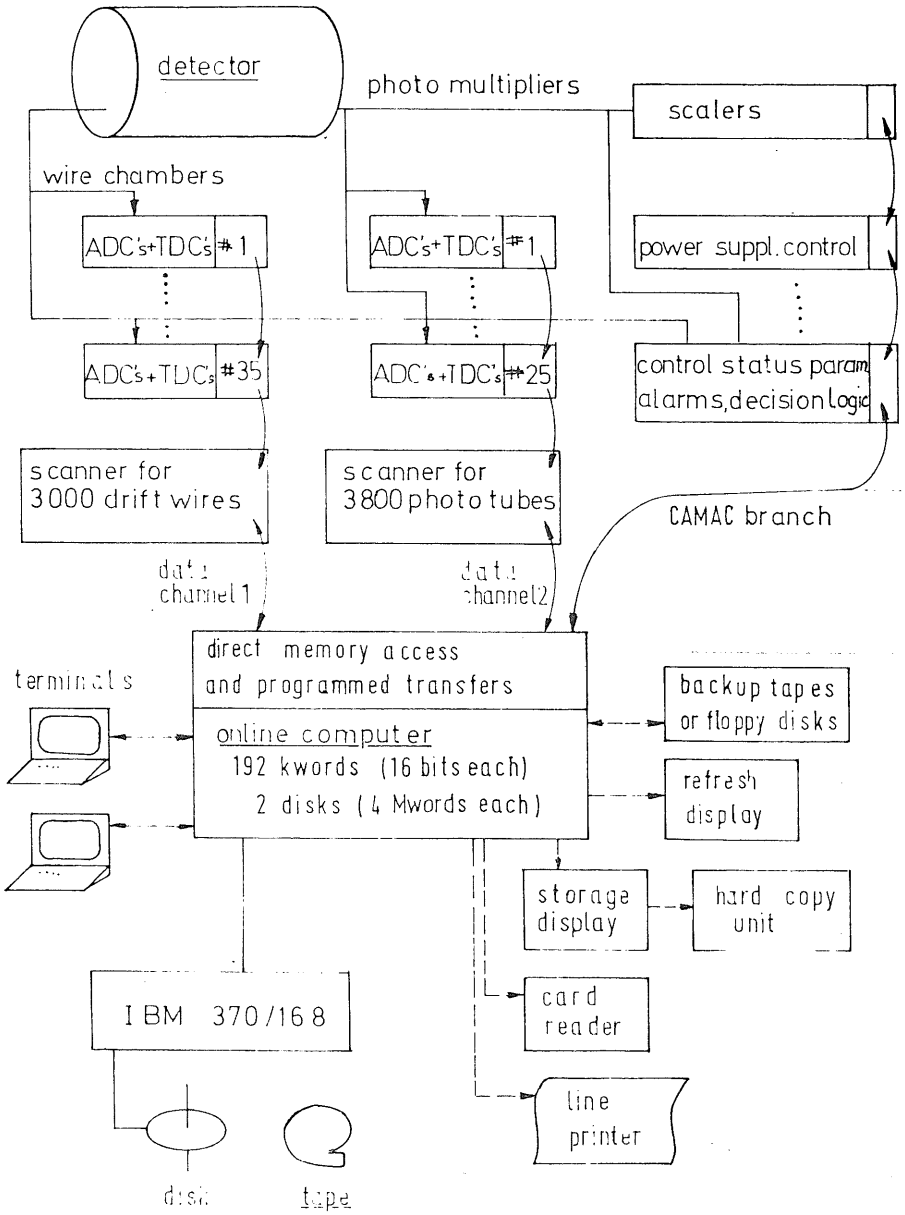

Fig.3.2

4 PHYSICS PROGRAMME

4.1 Total Cross Section Measurement

A useful measurement of the total annihilation cross section requires a high precision experiment. This is evident from the following considerations. Present experimental evidence at center-of-mass energies W below 7 GeV indicates that the ratio R between the total hadronic cross section and the μ-pair cross section is of the order

$$R = \frac{\sigma_{tot}(e^+e^- \to \text{hadrons})}{\sigma(e^+e^- \to \mu^+\mu^-)} \simeq 6$$

If a new heavy lepton pair is produced, the ratio R is expected to change by one unit yielding a 16% change in the total cross section. Therefore an experiment sensitive to these effects has to measure the total cross section with an accuracy of about 5%. A similar step due to the production of new hadrons is expected to be even smaller unless it is amplified by resonance enhancements near threshold.

The accuracy achievable in a total cross section measurement depends on the one hand on the knowledge of the systematic uncertainties such as trigger- and detection efficiency, luminosity etc., and on the other hand on how well the two-photon processes (I) can be separated from genuine one-photon annihilation events (II).

$$e^+e^- \to e^+e^- + \text{hadrons} \quad \text{(I)}$$

$$e^+e^- \to \text{hadrons} \quad \text{(II)}$$

As indicated in fig. 4.1 the diffractive contribution from reaction (I) is about 10 times larger than the total cross section for reaction (II) at 15 GeV beam energy. The two-photon diffractive cross

section in fig. 4.1 was calculated according to Gatto and Preparata (1)

$$d\sigma(e^+e^-\to e^+e^- + X) = \int_0^E \frac{d\omega_1}{\omega_1}\frac{d\omega_2}{\omega_2} N(\omega_1)\, N(\omega_2)\, \sigma_{\gamma\gamma\to X}(W_{\gamma\gamma}) \qquad (4.1)$$

where $N(\omega_{1,2})$ are the virtual photon spectra carried by the $e^+(e^-)$ beams. The meaning of the other kinematic variables in eq. (4.1) may be read from fig. 4.2. The cross section $\sigma_{\gamma\gamma}(W_{\gamma\gamma})$ is estimated to be (2)

$\sigma_{\gamma\gamma} = 0.24\mu b + 0.27\mu b\ \mathrm{GeV}/W_{\gamma\gamma}$.

A Monte Carlo simulation of the experiment was performed in order to estimate the background of two photon events beneath the annihilation events. One-photon annihilation events were generated according to a phase space model with charged and neutral multiplicities of 8.0 and 4.0, respectively, at 15 GeV beam energy. On the average 1.5 K_L^o were produced per event, all other particles were assumed to be pions. For the two photon events we assumed an invariant mass distribution according to eq. (4.1) with charged multiplicities varying like

$$n_c = 1.86 + 1.56 \ln W_{\gamma\gamma}$$

and average neutral multiplicities of half that value. Here all particles were pions with a transverse momentum cut-off according to

$$\left(\frac{d\sigma}{dp_\perp}\right)_{\gamma\gamma} = \exp\left(-p_\perp/0.4\ \mathrm{GeV}\right).$$

Concerning the detector the following assumptions were made:

1) only particles within the range $20^o \le \theta \le 160^o$ were accepted,

2) a charged particle momentum resolution of $\frac{\Delta p}{p} = \pm\, 0.02 \cdot P(\mathrm{GeV/c})$

3) a photon energy resolution of $\frac{\sigma_E}{E} = \pm\, 0.06/\sqrt{E}$. The distribution of

the measured energy is shown in fig. 4.3. The two processes are well separated. If appropriate cuts are introduced the losses of genuine one photon events and the two-photon background are each less than 2%. These corrections will be well known since we measure the curve shown in fig. 4.3 directly and since some (≈ 5%) of the two-photon events are labelled by the tagging system. We conclude that the proposed apparatus is able to separate completely two-photon events from single photon annihilation.

The systematic uncertainties of our detection system are expected to be small. The detection efficiency is close to 100% due to the large solid angle for charged particles and photons. The envisaged trigger will not introduce any significant bias. The normalization will be obtained from the small angle luminosity monitor and, once the validity of Q.E.D. has been established with sufficient accuracy, with the help of the e^+e^-- and $\mu^+\mu^-$-events measured in the central detector.

To estimate the expected rates, we assume R ≈ 6 and an average luminosity of $L = 5 \times 10^{30}\mathrm{cm}^{-2}\mathrm{sec}^{-1}$. Using these numbers we expect in a 4π solid angle 40 μ-pairs/day and 240 hadronic events/day at E = 15 GeV. This is sufficient to perform accurate measurements of σ_{tot} at several energies and possibly also a fine scan over a limited energy range in the first series of experiments.

4.2 Search for New Particles in Leptonic Final States

4.2.1 Introduction

Following the recent discoveries of new particles (3) in pp and e^+e^- and ν reactions it is important to answer the questions:

a) Will more new quantum numbers (e.g. flavours) be excited in sequence as we move to higher energies?

b) Are there more leptons of higher mass?

PETRA is well suited to investigate these questions since new leptons or hadrons, if either they or their constituents possess a point-like charge, will be copiously pair-produced in e^+e^- annihilation under relatively clean background conditions.

A high value of R or an irregularity (spike, bump or shoulder) in the energy dependence of R could be an indication of the production of new particles. A clean way of detecting a new weakly-decaying particle is to observe its leptonic or semi-leptonic decay. For example a heavy lepton $L^\pm$ will decay into $\nu_L e^\pm \nu_e$, $\nu_L \mu^\pm \nu_\mu$ or ν_L + hadrons, whilst a new hadron $H^\pm$ with a new flavour will decay into $\nu_e e^\pm$ + hadrons, $\nu_\mu \mu^\pm$ + hadrons or purely hadronically.

The pair-produced new particles can therefore be searched for either in channels containing one charged lepton or in channels containing a pair of charged leptons. The dilepton events occur when both members of the pair decay either leptonically or semi-leptonically and thus have a lower rate than the single lepton event, but backgrounds are expected to be much smaller.

4.2.2 Expected Signal in Single Lepton Channel

a) Expected signal due to heavy leptons $L^\pm$:

Well above the production threshold the cross section for heavy lepton pair production should tend rapidly to the point-like cross section $\sigma = \frac{80}{W^2}$ nb (W in GeV) which is about 0.09 nb at W = 30 GeV. The branching ratio for each of the heavy lepton decay channels $L \to e\nu_L\nu_e$, $L \to \mu\nu_L\nu_\mu$ is expected to be approximately (4) $(R + 2)^{-1}$ which is about 0.15 for R = 5. The expected cross section for each of the processes $e^+e^- \to L^+L^- \to \begin{pmatrix} e^\pm \\ \mu^\pm \end{pmatrix}$ + anything is then 2 x 0.09 x 0.15 = 0.027 nb which gives an event rate of 12 events per day for a luminosity of 5×10^{30} cm^{-2} sec^{-1}. Curve 1 of fig. 4.4 shows the expected lepton momentum spectrum obtained assuming a V - A decay of a heavy lepton of mass 12 GeV/c^2 produced by 15 GeV beams.

b) Expected signal due to new hadrons $H^\pm$:

Here it is more difficult to make predictions. The cross section for the reaction $e^+e^- \to H^+H^-$ is hard to estimate. There would probably be a resonance enhancement just above the threshold similar to those seen in $e^+e^- \to K\bar{K}$ at the Φ mass and in the total annihilation cross section near 4 GeV. If this enhancement is ΔR times the point-like cross section, and the semi-leptonic branching ratio of the $H^\pm$ is B, then the single electron or muon cross sections are 0.18 x ΔR x B nb, which is equal to the cross sections from heavy leptons if ΔR x B is 0.15.

The lepton momentum spectrum is also difficult to calculate. We might naively expect the leptons to tend to have less momentum than those from heavy lepton decay, since the decay of a heavy hadron would most likely contain several hadrons having a high effective mass.

To get some idea of the shape of the momentum spectrum we considered the case of a 14 GeV/c^2 hadron decaying via the V-A interaction into a system containing hadrons of effective mass 7 GeV/c^2. The parent and the final state hadronic system were both treated as if they were point-like spin $\frac{1}{2}$ particles*). The results obtained assuming $\Delta R \times B = 0.4$ are shown in curve 2 of fig. 4.4

4.2.3 Backgrounds in the Single Electron Channel

The main sources of background in the electron channel are the following:

a) Asymmetric Dalitz pairs from π^o decay

b) Asymmetric e^+e^- pairs from γ conversion in the beam pipe

c) Hadron misidentification

d) Photon-photon interactions

e) Beam-gas interactions

Asymmetric pairs from processes a) and b) are the dominant backgrounds for electron momenta below 1 GeV/c. These narrow angle e^+e^- pairs will be widened by the magnetic field and can usually be rejected. A low momentum electron from a very asymmetric pair, however, might curl round before reaching the drift chambers and might

---

* We note that a similar procedure gives a reasonable fit to the electron momentum spectrum observed at DORIS at W = 4.1 GeV/c^2 if a parent mass of 1.9 GeV/c^2 and a final hadronic mass of 0.95 GeV/c^2 are used.

escape detection. Our lower momentum cut off is as low as 25 MeV/c for the Dalitz pair and 12 MeV/c for the pair converted in the beam pipe due to the low magnetic field of 5 KG and the dense chamber sampling close to the beam pipe. This helps to minimize the backgrounds.

Another background comes from hadron misidentification. A comparison of the momentum of a particle with the energy which it deposits in the leadglass counters provides a hadron rejection factor better than 300 for momenta greater than 2 GeV/c.

Rates for the backgrounds a), b), c) were calculated using the hadron momentum spectrum obtained from a jet model (5) with the pessimistic assumption that all particles are pions. Average charged and neutral pion multiplicities were both taken to be 8. The total annihilation cross section was assumed to be 6 times the point-like cross section. The results are shown in curve 3 of fig. 4.4

The backgrounds from photon-photon and beam-gas interactions are expected to be much smaller than above for an electron angle larger than 30^o. In any case these backgrounds have a sharp angular distribution peaking towards the beam direction and can easily be recognized.

As seen in fig. 4.4, the expected signals have flat momentum distributions distinctively different from the steeply decreasing background distributions. A clean signal can be expected for electron momenta above a few GeV/c. It should also be noticed that the backgrounds from very asymmetric Dalitz or γ-converted pairs can be estimated from the rate of "not so asymmetric pairs" observed in the inner detector. An improvement of a factor of 10 or more in the hadron rejection factor can also be expected from dE/dX measurement in the

drift chambers. Our detector therefore probably has sufficient redundancy against the electron backgrounds to allow signals a factor 10 weaker thean those indicated in fig.4.4 to be observed.

4.2.4 Backgrounds in the Single Muon Channel

The main backgrounds in the single muon channel are due to hadron punch through and hadron decay. Between the interaction point and the end of the μ-filter there is a total of 6 to 8 absorption lengths of material depending on the angle. This gives a punch-through probability of less than 2×10^{-3}. Most of the $K^{\pm}$ decays can be rejected by track measurements in the muon filter. This has already been discussed in section 2.6. The expected momentum distribution from these backgrounds was calculated using the charged hadron momentum spectrum from the above-mentioned jet model. Equal numbers of $\pi^{\pm}$, $K^{\pm}$ were assumed. Measured momentum dependent absorption lengths (6) were used. The results are shown in fig. 4.5. The situation is similar to that in the single electron channel. The expected signals can be well separated from the steeply falling background for momenta above a few GeV/c.

4.2.5 The Dilepton Channels

A study of the dilepton channels will provide further important information. A comparison of the rates in the ee, eμ and μμ channels, for example, gives the branching ratio B_e/B_μ which could be used to distinguish between a sequential heavy lepton and a heavy lepton with electron-or muon-number (heavy lepton of Georgi-Glashow type (7)).

The observation of the "dilepton + hadrons" channel would prove that the new particle was a hadron.

The cross sections for the dilepton channels are $0.09 \times \Delta R \times B^2$ nb. at W = 30 GeV for each of the ee and μμ channels and twice that value for the eμ channel. For the sequential hevy lepton $L^{\pm}$, this gives a total cross section of 8 pb for all dilepton channels, corresponding to 3.5 events/day at an average luminosity of $5 \times 10^{30} cm^{-2}\ sec^{-1}$. The background situation is rather clean for the dilepton channels. A signal/background ratio of about 100 is expected if each lepton has a momentum greater than 2 GeV/c.

4.2.6 Other New Particles

The above discussions concentrated on the sequential charged heavy lepton and the new weakly decaying hadrons. Any new weakly decaying particle, however, is expected to have leptonic or semileptonic decays. This is the case for heavy leptons $E^{\pm}$, $M^{\pm}$ of the Georgi-Glashow type, for neutral heavy leptons, for the weak intermediate boson $W^{\pm}$, and for the Higg's scalar ϕ. All these "conventional" new particles as well as any yet unconceived new ones could be searched for with our apparatus.

4.3 Q.E.D. Reactions and Weak Interaction Effects

Our apparatus has excellent properties for measuring the classical Q.E.D. processes

$$e^+e^- \to \mu^+\mu^- \qquad \text{(I)}$$
$$e^+e^- \to e^+e^- \qquad \text{(II)}$$
$$e^+e^- \to \gamma\gamma \qquad \text{(III)}$$

At PETRA energies the processes (I) and (II) offer a unique opportunity not only to perform significant tests of Q.E.D. but also to study weak interactions in the absence of hadrons through the interference between the electromagnetic and the weak neutral current. With longitudinally and transversely polarized beams the full determination of the weak interaction coupling constants $g_{A,V}^{e,\mu}$ is feasible in principle (8). Since in the first round of experiments there will be at most only transversely polarized beams, we consider only the effects of transverse beam polarization. Weak and electromagnetic effects have to be disentangled by comparison of the reactions (I) - (III) and their s-dependences.

4.3.1 $e^+e^- \to \mu^+\mu^-$

Assuming time-reversal invariance the differential cross section (to first order in Q.E.D.) for reaction (I) is given by

$$\frac{d\sigma}{d\Omega} = \frac{\alpha^2}{4s}\left\{\left(1 + \frac{s\cdot Re(g_e^{V*} g_\mu^{V})}{2\pi\alpha(s-M_z^2)}\right)\left(1 + \cos^2\theta - P_+^T P_-^T \sin^2\theta\cos 2\phi\right) + \frac{s\cdot Re(g_e^{A*} g_\mu^{A})}{\pi\alpha(s-M_z^2)}\cos\theta\right\}$$

where g_A and g_V are the axial-vector and vector coupling constants, and M_Z is the mass of the neutral weak vector boson Z_o. The weak vector term changes the absolute rate from the Q.E.D. value, while the axial vector term introduces a charge asymmetry.

$$A = \frac{d\sigma(\theta) - d\sigma(\pi-\theta)}{d\sigma(\theta) + d\sigma(\pi-\theta)}$$

The actual values of g_V and g_A are strongly model dependent. For the standard V - A theory a - 16% change of the total rate relative to Q.E.D. is predicted at 15 GeV beam energy. For the Weinberg-Salam-model the effect depends strongly on the mixing angle, $\theta_W = 35^o$ yielding about - 1%. The predicted asymmetries are plotted in fig. 4.6. The asymmetries are sensitive to the transverse beam polarization, which therefore has to be continuously monitored. This can be done with the help of the reaction $e^+e^- \to \gamma\gamma$ discussed later.

Experimentally reaction (I) can be easily identified in the angular range $25^o \leq \theta \leq 155^o$, by demanding two nearly collinear tracks, each with an energy equal to the beam energy and passing through the μ-filter. Clear charge determination is possible in this angular range (see fig. 1.1), and the inner detector as well as the μ-detector provide sufficient redundancies not to introduce any bias to the asymmetry measurements. A complication is caused by higher-order electromagnetic effects which also yield some charge asymmetry. This asymmetry depends on the various experimental cuts. It has been estimated by Berends et al. (9) to be of the order of a few % in the range $45^o < \theta < 90^o$ but increasing to

about 20% at $\theta = 5^{o}$. This asymmetry is roughly independent of energy and can therefore be separated from the weak interaction effects (being proportional to s as long as $s << M_Z$) by studying carefully the s-dependence.

The expected rates in our detector are listed in the table below. A detailed study of the weak-electromagnetic interference effects needs accurate measurements at at least two different energies, one of which should be the maximum one.

4.3.2 $e^+e^- \to e^+e^-$

The e^+e^- final state is more complicated to describe due to the presence of the t-channel exchange diagrams. For the cross section formula we refer to the work of Budny and McDonald (10). The expected rates due to weak interactions normalized to the Q.E.D. values are plotted in fig. 4.7. Rate effects of a few % can be expected in certain angular ranges at E = 15 GeV.

Experimentally e^+e^- events are easily detected in the range $25^{o} \leq \theta \leq 155^{o}$ and identified by the high signals in the leadglass counters. The expected rates are listed in the following table:

Process	Rates
$e^+e^- \to e^+e^-$	3.6×10^5
$\to \mu\mu$	8.0×10^3
$\to \gamma\gamma$	2.6×10^4

Rates of Q.F.D. processes in our detector $25^{o} \leq \theta \leq 155^{o}$, $0^{o} \leq \phi \leq 360^{o}$ for an integrated luminosity of $L = 10^{38}$ cm^{-2} at beam energies of E = 15 GeV.

4.3.3 $e^+e^- \to \gamma\gamma$

No sizeable contributions from weak interactions are expected for the two photon final state. The first order cross section is

$$\frac{d\sigma}{d\Omega} = \frac{\alpha^2}{s \cdot \sin^2\theta} \left(1 + \cos^2\theta + |P_+^T| \cdot |P_-^T| \cdot \sin^2\theta \cdot \cos 2\phi \right)$$

This process provides a sensitive long term monitor of the beam polarization as is seen from fig. 4.8, where the ϕ dependence of $d\sigma/d\Omega$ is plotted for various values of the transverse beam polarization. Experimentally the $(\gamma\gamma)$-final state is clearly identified by the two large signals in the leadglass counters. Our experiment will thus perform a clean check of the Q.E.D. predictions. If no Q.E.D. violation occurs at the highest PETRA energies we will be capable of increasing the usual cut-off parameter Λ by a factor of 5.

4.3.4 Weak Interaction Effects in $e^+e^- \to$ hadrons

It has been suggested that weak interaction effects will show up in inclusive hadron spectra for hadrons with $x = 2p/\sqrt{s} \geq 0.3$ (11). The asymmetry and polarization effects are expected to be of the same order of magnitude as for μ-pair production. In addition one might investigate the correlations between inclusive hadron momenta and helicities, to find or exclude possible contributions from S, P or T couplings. The Λ particle is a particularly useful probe in searching for polarization effects in the final state.

4.4 Study of Hadronic Final States

In addition to the total cross section (see section 4.1) we intend to investigate more detailed features of the hadronic final states. The large solid angle for the measurement of charged particle momenta and for the measurement of the energy and direction of γ-rays should allow the reconstruction of simple exclusive reaction channels with good efficiency.

A parton-like structure in e^+e^- annihilation manifests itself in the distribution of the final state hadrons: One expects a so-called 'back-to-back' jet structure (12). Experimentally multihadron events of the jet type are difficult to resolve since the tracks are hard to disentangle in conventional drift chambers.

Our inner detector has features (see section 2.3) which help to overcome these difficulties. We measure the azimuthal angle and z coordinate of each particle at 50 points along its track and can resolve adjacent tracks which are separated by more than 3mm in the azimuthal coordinate. As can be seen from figures 4.9 and 4.10 these features make track tracing easy even for jet-like events. Less than 10% of all jet-like events have tracks which cannot be unambiguously reconstructed.

Figure 4.11 illustrates how well we can distinguish between jet-like events and isotropic events by making a sphericity plot for the charged tracks.

A study of single particle inclusive momentum spectra will also be possible. Measurements in the energy range 3.0 GeV $\leq \sqrt{s} \leq$ 7.4 GeV have shown (12) that the cross section $s \cdot d\sigma/dx$ scales for $x \geq 0.4$.

x is the scaling variable defined as $x = 2p/\sqrt{s}$, where p is the momentum of the charged particle.

We have calculated the expected rate assuming that for $x \geq 0.4$ Bjorken scaling still holds (even for $\sqrt{s}$ = 30 GeV) and that below x = 0.4 the cross section will tend to the asymptotic limit taken to be $s \cdot d\sigma/dx = 31 \cdot \exp(-7.7 \cdot x)$. The results are given for a mean luminosity of $\langle L \rangle = 5 \cdot 10^{30}$ sec^{-1} cm^{-2} in the following table.

Estimated yield of charged hadrons per day at $\sqrt{s}$ = 30 GeV, $L = 5 \cdot 10^{30}$ sec^{-1} cm^{-2}

$x = 2p/\sqrt{s}$	p (GeV/c)	number of charged hadrons in $\Delta x = \pm 0.05$
0.1	1.5	680
0.2	3	310
0.3	4.5	140
0.4	6	64
0.5	7.5	39
0.6	9	23
0.7	10.5	13
0.8	12	9
0.9	13.5	5

With a mean charged multiplicity of $\langle n_{ch} \rangle = 7.5$ the integral over the full range $0 < x < 1$ corresponds to approximately 240 hadronic events/day.

A single particle trigger should not be necessary for the measurement of inclusive spectra since the acceptance of the apparatus for charged particles and γ-rays is close to 100%.

The high spatial resolution of the inner detector also plays an important role in detecting V particles in the final state. Identification of individual hadrons is possible up to 0.6 GeV/c with the time-of-flight method and up to 0.7 GeV/c by the dE/dx measurement in the drift chamber. Possibly also in the higher momentum range 2 to 7 GeV/c π/K separation may be possible using the dE/dx values.

4.5 $e^+e^- \rightarrow e^+e^-$ + hadrons

4.5.1 Introduction

Much of the physics done at electron-positron storage rings has involved the single photon annihilation channel. However at the new machines (PETRA, PEP), operating in a higher energy regime, the two-photon process (see fig. 4.2 for notation) will provide events at comparable rates.

The two-photon process has been thoroughly discussed both theoretically(2,13,14)and at the Berkeley summer studies from an experimenter's point of view(15,16). The physics is done by tagging the scattered electron and the scattered positron in coincidence using suitable identification apparatus placed close to the beam pipe on either side of the interaction point. Final state particles, leptons or hadrons, are found in general in the central detector.

4.5.2 Photon-Photon Collisions

Our tagging system restricts the electron, positron scattering to angles less than 80mr so that except for a small $W_{\gamma\gamma}$ q_1^2 (photon four-momentum squared) and q_2^2 will be less than $1(\mathrm{GeV/c})^2$. Thus both photons are almost real and we are studying the hadronic characteristic of photons much as one might do with a ρ^o,ρ^o storage ring. However it is certain that the photon has specifically non-hadronic characteristics and these properties are likely to change rapidly in the region between $q^2 = 0$ and $q^2 = 1(\mathrm{GeV/c})^2$. The trigger for a γ-γ interaction will be a double tag with $1 < E_1, E_2 < (E - 1)$ GeV and at least one hadron or photon in the central detector. (We can also examine Q.E.D. processes like

$e^+ + e^- \to e^+ + e^- + e^+ + e^-$, or $\to e^+ + e^- + \mu^+ + \mu^-$, or $\to e^+ + e^- + \gamma + \gamma$, by observing a double tag plus two electrons, or muons, or photons in the central detector.) The rates will be acceptable since the "$\gamma\gamma$ luminosity" varies only logarithmically with θ_1 and θ_2. In the table below we show the total number of hadronic $\gamma\gamma$ events expected in the tagging system under the assumption that the cross section for $\gamma+\gamma \to$ hadrons is of the form $\sigma_{\gamma\gamma} = 0.24 + \frac{0.27}{W_{\gamma\gamma}}$ μb. The rates are calculated for intervals of 1 GeV in $W_{\gamma\gamma}$ and for an integrated luminosity of 10^{38}cm^{-2}. No correction is made for small changes in photon structure functions as q^2 increases to $1(\text{GeV/c})^2$.

$W_{\gamma\gamma}$	5	10	15	20	25	Total $W_{\gamma\gamma} > 2.5$ GeV
Events per GeV	160	120	34	16	8	1720
($\int L_{ee} dt = 10^{38}\ \text{cm}^{-2}$)						

$\gamma + \gamma \to$ hadron event rate, E = 15 GeV

$30 < \theta < 80$mr. $1 < E_1, E_2 < 14$ GeV

The distribution of final states in the laboratory system is discussed in some detail in ref. 16. The important features are that the bulk of final-state particles appears at large angles to the beam direction. Only relatively few particles - those belonging to the fragmentation of the more energetic photon - will appear at smaller angles. A large fraction of all final state hadrons in γ-γ events will therefore appear in the central detector enabling us to study the usual inclusive distributions, correlations with high $p_\perp$ events, etc. even with relatively few events.

We can see immediately from Table II that the total number of

photon-photon hadronic events with total energy greater than 20 GeV is about 80 corresponding to an integrated luminosity of 10^{38}cm^{-2}. This is adequate to calculate the total photon-photon "background" in the single-photon annihilation channel. Two-photon processes with an energy $W_{\gamma\gamma} \lesssim 2.8$ GeV cannot be identified positively in the tagging system, as the electrons cannot be distinguished from Bhabha scatters because of the limited resolution of the lead glass counters. However, exclusive processes, esp. narrow resonance production can still be analysed in our central detector.

4.5.3 Deep Inelastic Electron-Photon Scattering

The two-photon process with one photon far off the mass shell gives us the opportunity to study further the structure of the photon. Conventionally we write the reaction as:

$e + \gamma \to e +$ hadrons

where $q_1^2 \lesssim 1\ \text{GeV}^2$ corresponds to the target photon

and $q_2^2 > 1\ \text{GeV}^2$ for the exchanged virtual photon.

Using our apparatus it will be possible to start looking at these processes by defining q_1^2 by the tagging system and detecting deep inelastic scatters by the central detector: $\theta > 200$mr. Naturally the rates will be very low but the virtual photon flux, after integrating over the range of real-photon energies, only falls as q_2^{-2}. Since the target photon is polarized the cross section can be expressed in terms of three structure functions. We estimate after some simple assumptions on the variation of these structure functions that the total number of events with $W_{\gamma\gamma} > 2$ GeV and $q_2^2 > 1(\text{GeV})^2$ is about 100 for an integrated luminosity of $10^{38}\ \text{cm}^{-2}$.

References

1) R. Gatto, G. Preparata, Nota Interna n. 441 (1973), Instituto di Fisica G. Marconi, Universita di Roma

2) S.J. Brodsky, Journal de Physique 35, C2-69 (1974)

3) J.J. Aubert et al., Phys. Rev. Lett. 33 (1974) 1404
J.E. Augustin et al., Phys. Rev. Lett. 33 (1974) 1406
M.L. Pearl et al., Phys. Rev. Lett. 35 (1975) 1483
J. Von Krogh et al., Phys. Rev. Lett. 36 (1976) 710
J. Blietschau et al., Phys. Lett. 60B (1976) 207
G. Goldhaber et al., LBL-5309, SLAC-1762, submitted to Phys. Rev. Letters
W. Braunschweig et al., DESY 76/37, submitted to Physics Letters
Pluto collaboration, contributed paper to 1976 Tbilisi Conference

4) For example Y.S. Tsai, Phys. Rev. D4 (1971) 2821

5) G. Hanson et al., SLAC-Pub.-1655, LBL - 4287

6) A. Grant et al., CERN/DPHII/75-42

7) H. Georgi, S.L. Glashow, Phys. Rev. D6 (1972) 429

8) PEP-Summer study 1975, page 31

9) F. Berends et al., Nucl. Physics B63, 381 (1973)

10) R. Budny, A. McDonald, Phys. Rev. D10 (1974) 3107

11) R. Gatto, G. Preparata, Nuovo Cimento Letters 7 (1973) 89

12) R.F. Schwitters, Proceedings of the 1975 International Symposium on Lepton and Photon Interactions, Stanford, p. 5

13) S.J. Brodsky, T. Kinoshita, H. Tevazawa, Phys. Rev. Lett. 27 (1971) 280

14) T.F. Walsh, Journal de Physique 35, C2 - 77 (1974)

15) Photon-Photon Physics, PEP Summer Study 1974

16) Photon-Photon Physics, PEP Summer Study 1975

Figure Captions

Fig. 4.1 Contributions to the two photon cross section as a as a function of beam enery

Fig. 4.2 Feynman diagram and notation for the two-photon process

Fig. 4.3 Monte Carlo results for the total measured energy distribution. K_L^o are assumed to escape detection.

Fig. 4.4 Expected electron spectra from new weakly decaying particles and estimated background

Fig. 4.5 Expected muon spectra from new weakly decaying particles and estimated background

Fig. 4.6 Charge asymmetries for $e^+e^- \to \mu^+\mu^-$

Fig. 4.7 Weak interaction effects on the $e^+e^- \to e^+e^-$ total cross section

Fig. 4.8 The ϕ-dependence of $\frac{d\sigma}{d\Omega}$ at different transverse beam polarizations for the reaction $e^+e^- \to \gamma\gamma$

Figs. 4.9 and 4.10 Monte Carlo generated jet events as seen in the internal detector

Fig. 4.11 Monte Carlo simulation : Sphericity of events with jet-like and isotropic distribution of charged tracks. p_i is the momentum of the i^{th} charged particle, $p_{\perp i}$ is the transverse momentum of the i^{th} charged particle with respect to the jet axis.

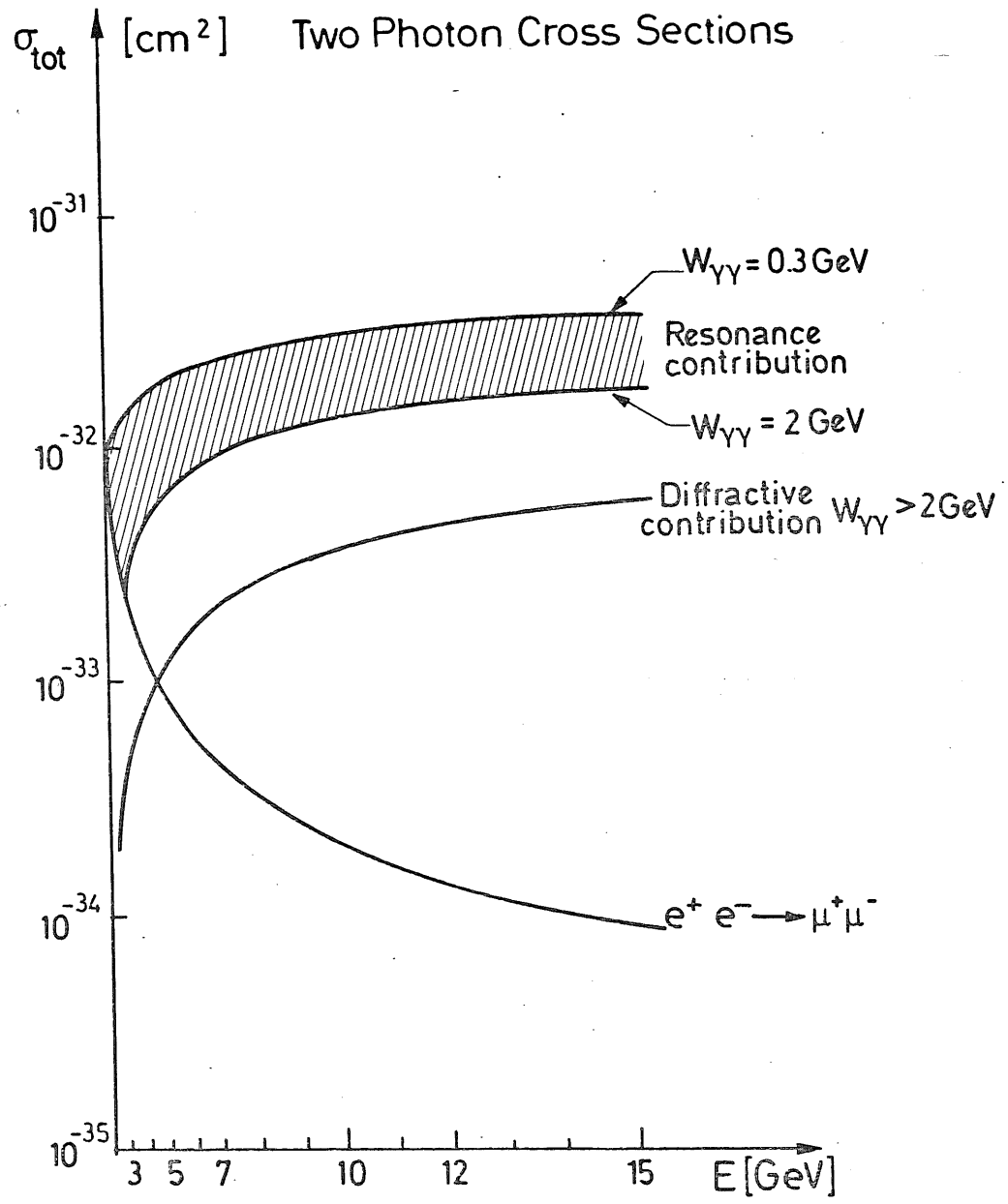

Fig. 4.1

2 Photon Process

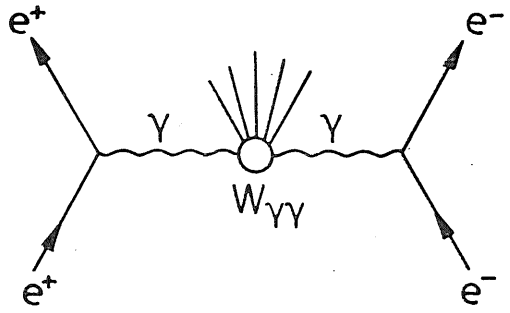

$e^+e^- \longrightarrow e^+e^- + X$

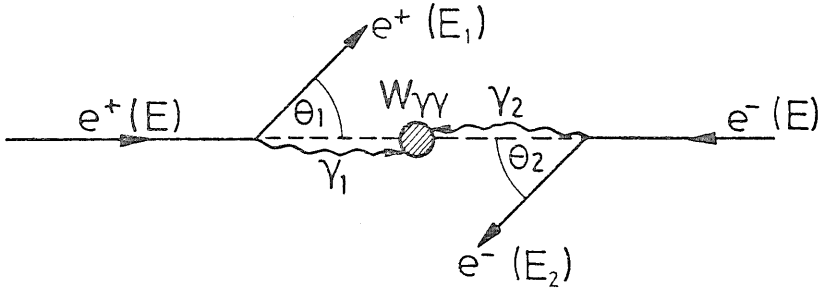

$\gamma_1 : (\vec{k}_1, \omega_1)$

$\gamma_2 : (\vec{k}_2, \omega_2)$

$W_{\gamma\gamma} \approx \sqrt{4\omega_1\omega_2}$

Fig. 4.2

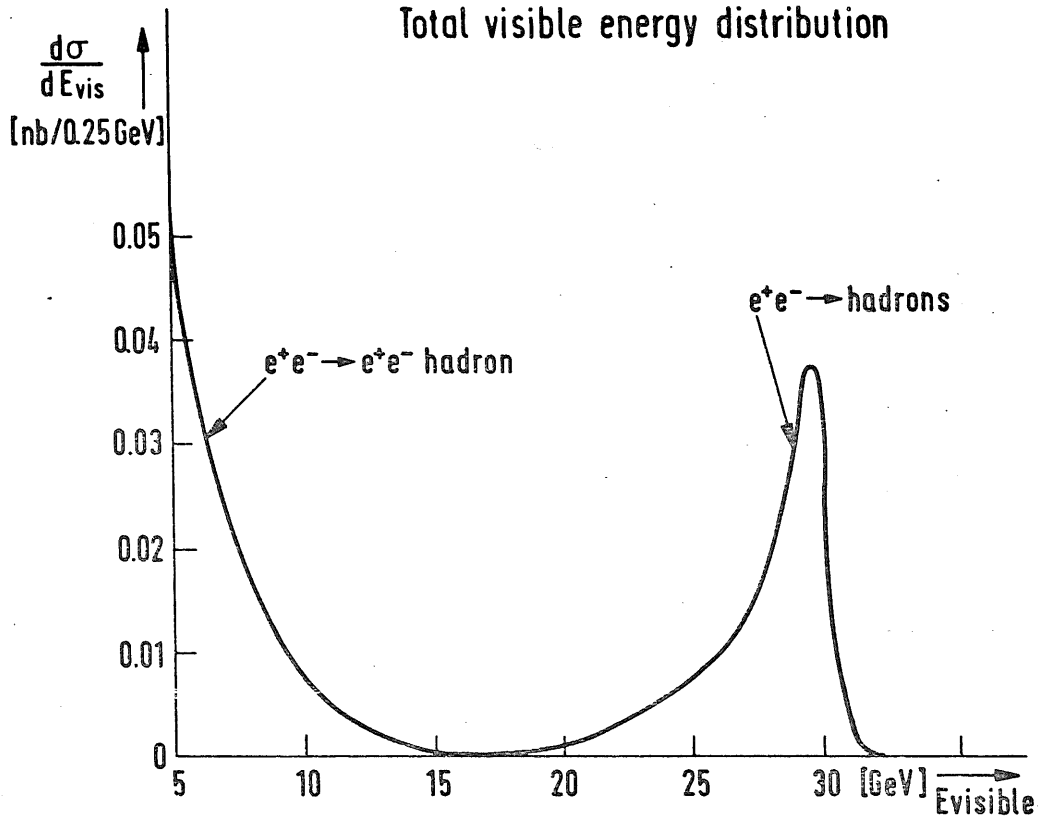

Monte Carlo with :

$\bar{E}_{beam} = 15$ GeV, $< n_{K^0_L} > = 1.5$/event

$\sigma_{\gamma\gamma}(s) = 0.24\,\mu b \div 0.14\,\mu b\,GeV/\sqrt{s}$

$\left(\frac{d\sigma}{dp_1}\right)_{\gamma\gamma} = \exp(-p_1/0.4\,GeV)$

$\Delta\Omega = 95\% \times 4\pi$

Fig. 4.3

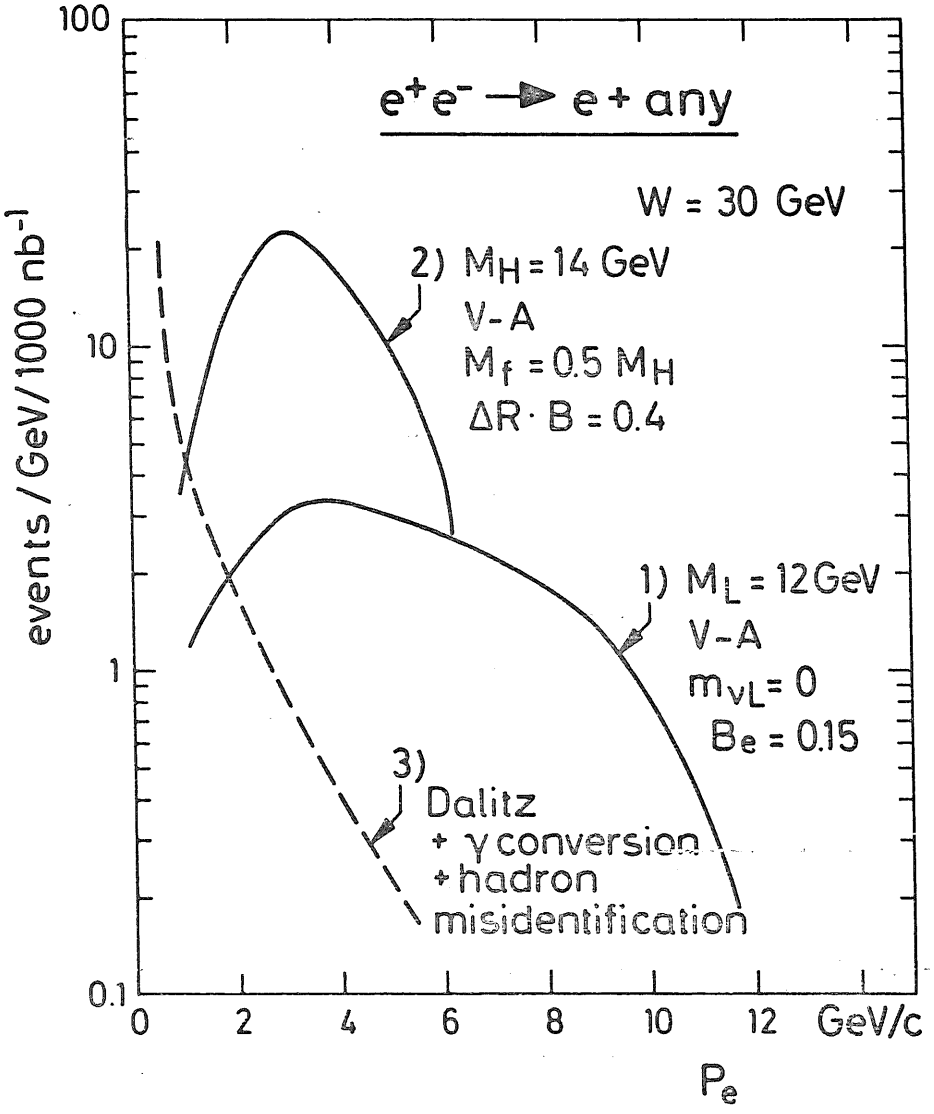
e+e− → e + any
W = 30 GeV
2) MH = 14 GeV
V-A
Mf = 0.5 MH
ΔR · B = 0.4
1) ML = 12 GeV
V-A
mνL = 0
Be = 0.15
3)
Dalitz
+ γ conversion
+ hadron
misidentification
events / GeV / 1000 nb-1
100
10
1
0.1
0
2
4
6
8
10
12
GeV/c
Pe

Fig. 4.4

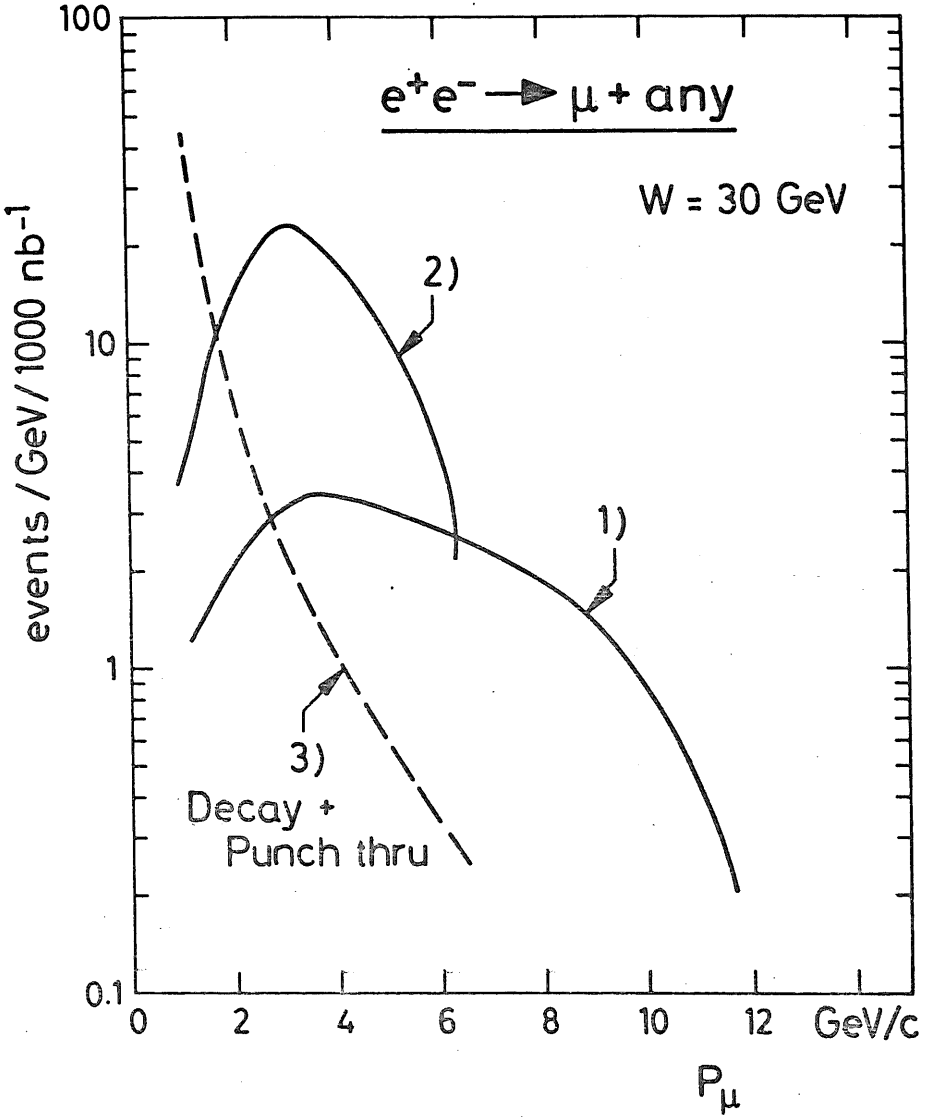
e+e− → μ + any
W = 30 GeV
2)
1)
3)
Decay +
Punch thru
events / GeV / 1000 nb-1
100
10
1
0.1
0
2
4
6
8
10
12
GeV/c
Pμ

Fig. 4.5

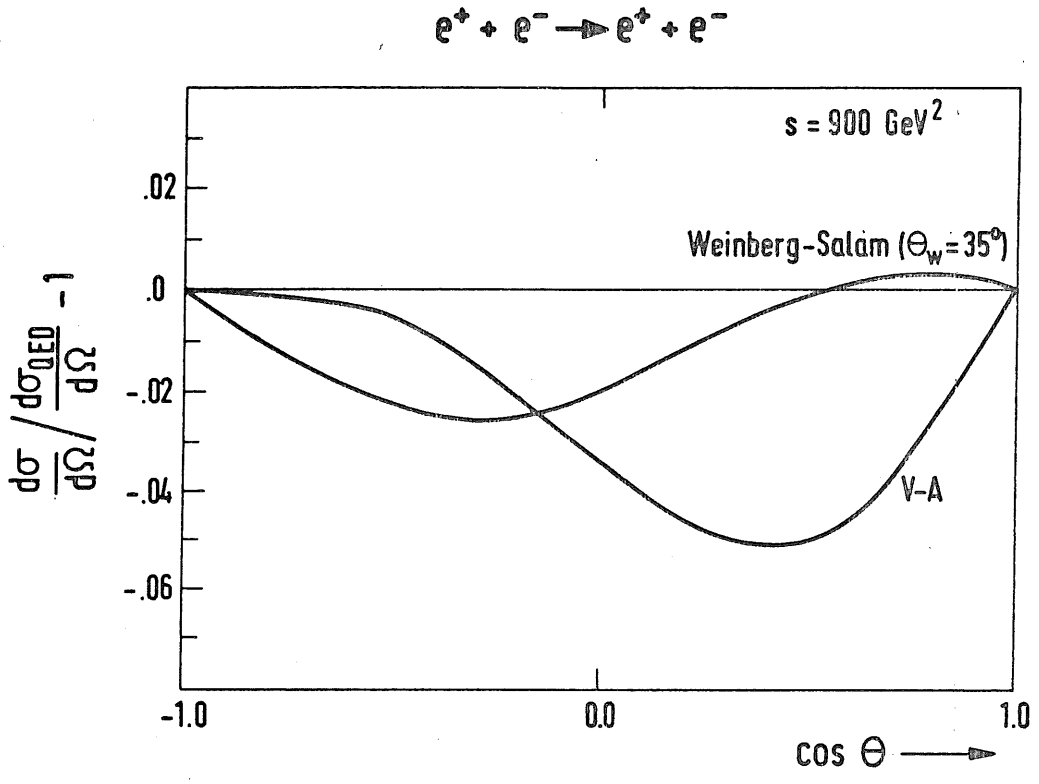
$e^+ + e^- \rightarrow e^+ + e^-$
s = 900 GeV^2
Weinberg-Salam ($\Theta_w = 35°$)
V-A
$\frac{d\sigma}{d\Omega} / \frac{d\sigma_{QED}}{d\Omega} - 1$
.02
.0
-.02
-.04
-.06
-1.0
0.0
1.0
cos Θ

Fig. 4.7

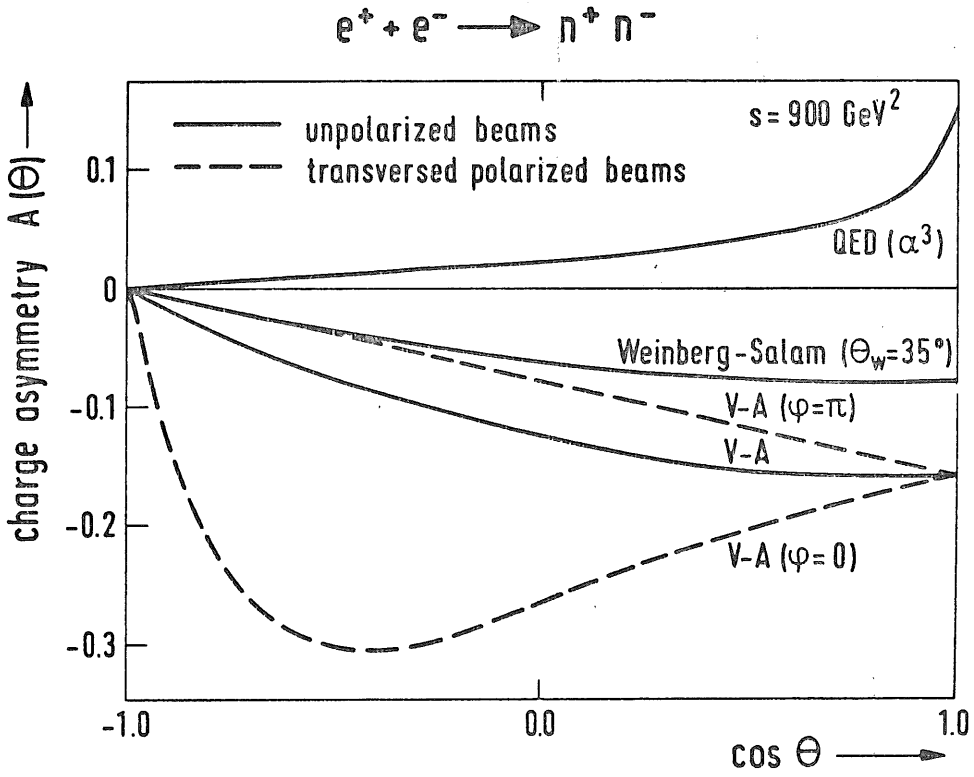
$e^+ + e^- \rightarrow \pi^+ \pi^-$
unpolarized beams
transversed polarized beams
s = 900 GeV^2
QED (α^3)
Weinberg-Salam ($\Theta_w = 35°$)
V-A ($\varphi = \pi$)
V-A
V-A ($\varphi = 0$)
charge asymmetry A(Θ)
0.1
0
-0.1
-0.2
-0.3
-1.0
0.0
1.0
cos Θ

Fig. 4.6

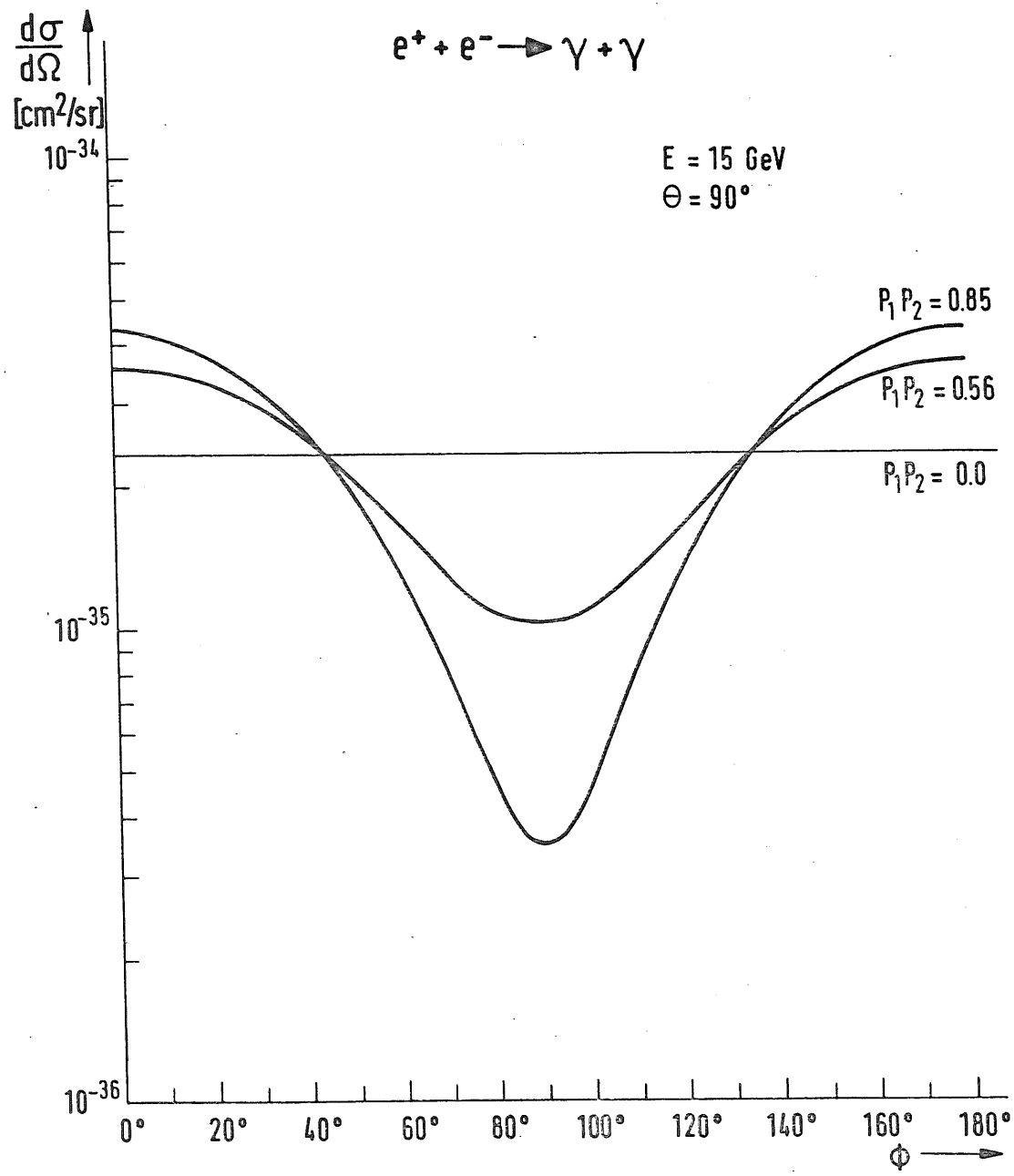
dσ/dΩ [cm²/sr]
e⁺ + e⁻ → γ + γ
E = 15 GeV
Θ = 90°
P₁P₂ = 0.85
P₁P₂ = 0.56
P₁P₂ = 0.0
10⁻³⁴
10⁻³⁵
10⁻³⁶
0°
20°
40°
60°
80°
100°
120°
140°
160°
180°
Φ

Fig. 4.8

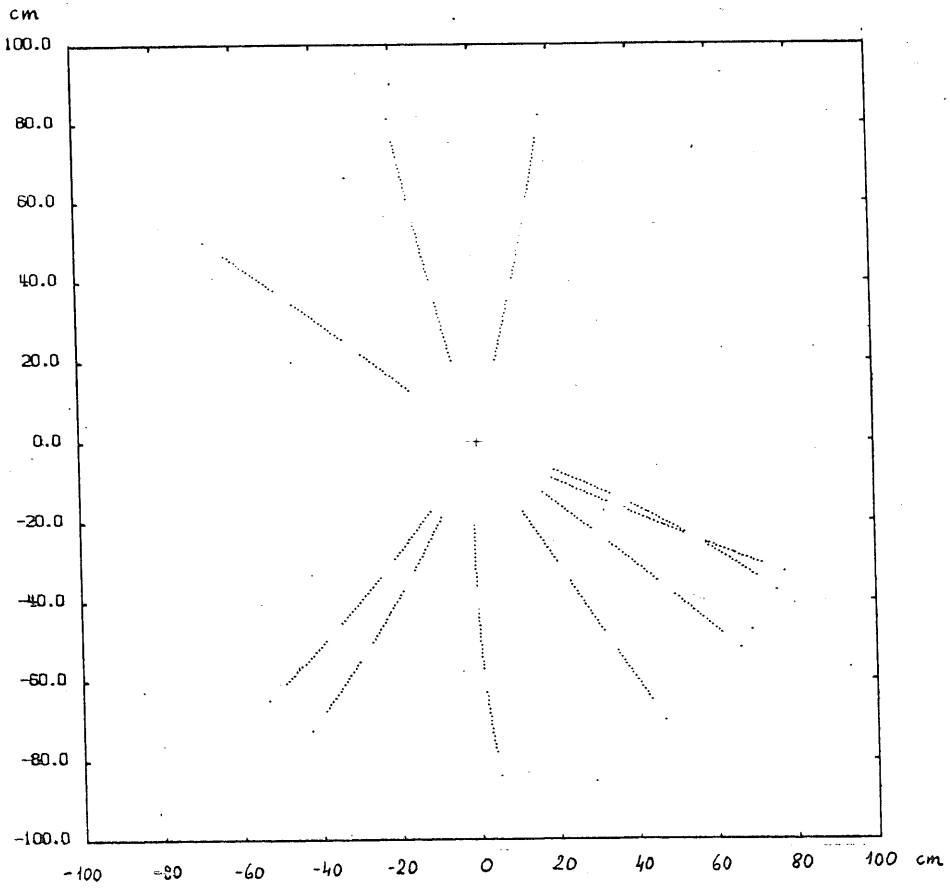
cm
100.0
80.0
60.0
40.0
20.0
0.0
-20.0
-40.0
-60.0
-80.0
-100.0
-100
-80
-60
-40
-20
0
20
40
60
80
100
cm

Fig. 4.9

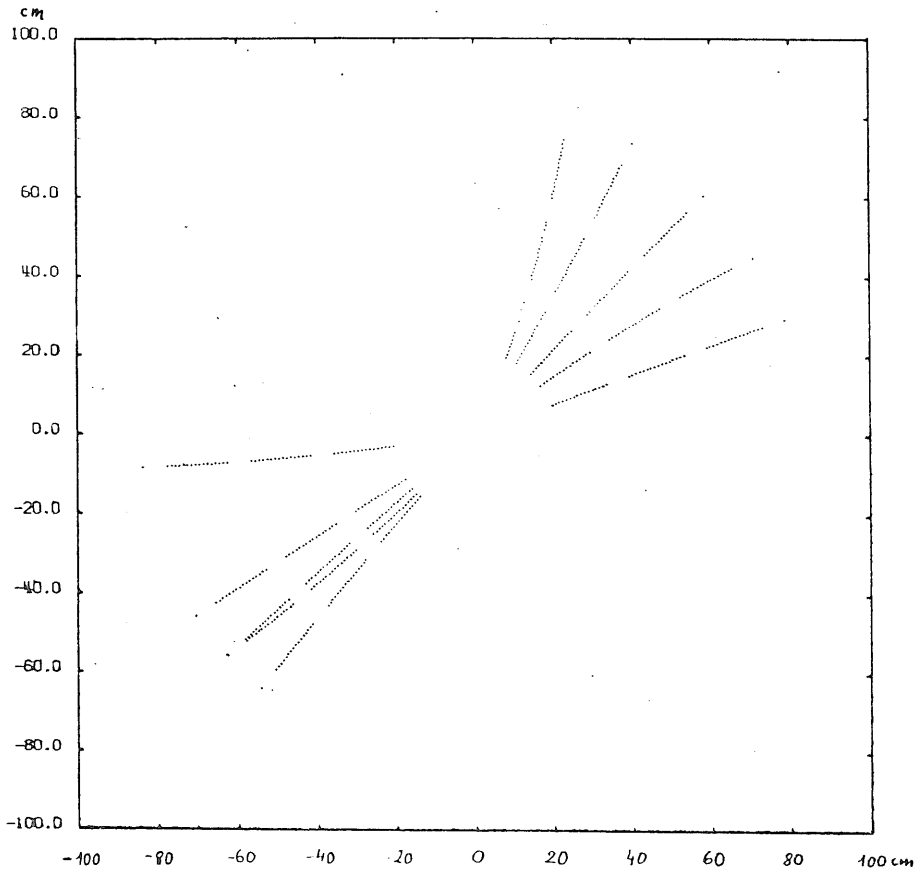

Fig. 4.10

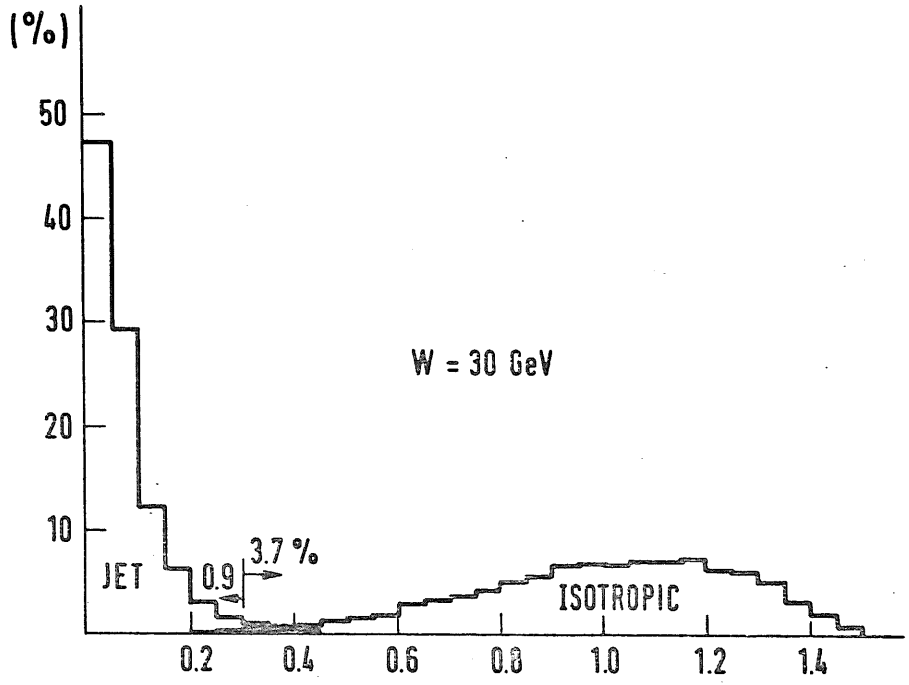

$$\text{Charged Sphericity} = \frac{3\,(\Sigma_i P_{ti}^2)}{2\,\Sigma_i P_i^2}$$

Fig. 4.11

5 EXPERIMENTAL ORGANIZATION

5.1 Work Sharing

The proposed division of work is based on the experiences and technical resources of the various groups. For details we refer to Table 5.1 where the main items are listed.

5.2 Cost Estimates

The cost estimates are also listed in Table 5.1. An exchange rate of 1 £ = 5 DM was assumed.

5.3 Time Schedule

Considering the time available before the first colliding beams at PETRA it is clear that the first contracts have to be placed shortly after the approval of the experiment.

In order to have the magnet ready to be shipped to DESY in June 1978 the contract has to be placed in February 1977. Since the design has therefore to be completed in 1976, an early decision on the proposal is essential. We have been assured that the leadglass and photo-tubes can be delivered within one year after order. The assembly of the leadglass counters has to start in the middle of 1977. Work on prototype drift chambers for the inner detector and the readout electronics has already been started. A full scale prototype of a jet-chamber module will be built until the end of 1976.

We are aware that a large amount of work must be done on software

development. First work on pattern recognition has already been started.

5.4 Space Requirements

The position of the proposed pit in the experimental hall is shown in fig. 5.1. The "closed" and "open" positions of the detector are indicated. A possible position of the counting house is also indicated. It has to have two floors in order to accomodate the electronics and the on-line computer. It is essential to have the power supply for the magnet located close to the coil since we use a high-current device.

5.5 DESY Services Required

The computer requirements have been specified in sec. 3.5. For the other items only crude estimates can be given. At present it is proposed that the detailed design and construction of the solenoid and the μ-filter will be in the hands of the Rutherford Laboratory. DESY services are required for: a) installation of the magnet power supply and cooling facilities, b) design and construction of the pit, foundations, counting house and shielding, c) final assembly of the detector, d) installation of the on-line computer. Furthermore the DESY part of the collaboration together with the University of Hamburg will take responsability for the beam-pipe, the compensating coils, the trigger and time-of-flight counters and the data acquisition.

Table 5.1

Item	Groups in Charge	Estimated Costs
beam pipe + pumps	DESY, Hamburg	350 k DM
magnet (coil + return yoke)	Daresbury	750
inner detector	Heidelberg	2.400
leadglass	Tokyo	4.500
μ-filter	Manchester	1.600 (2.600 if iron)
γγ-tagging	Lancaster	450
time-of-flight + trigger counters + electronics	DESY, Hamburg	800
data acquisition	DESY	1.350
compensating coils	DESY, Hamburg	100
pits + foundation + rails	DESY	400
counting house + installation	DESY	200
Installation of magnet power supply	DESY	300
cooling facilities	DESY	200
		13.400
contingency (10%)		1.300
Total		14.700 k DM

Figure Captions

Fig. 5.1 Plan view of an experimental hall showing the location of the proposed pit with the detector in the closed position (a) for data taking and in the open position (b) for setup and maintenance. A possible location of the is counting house is also shown.

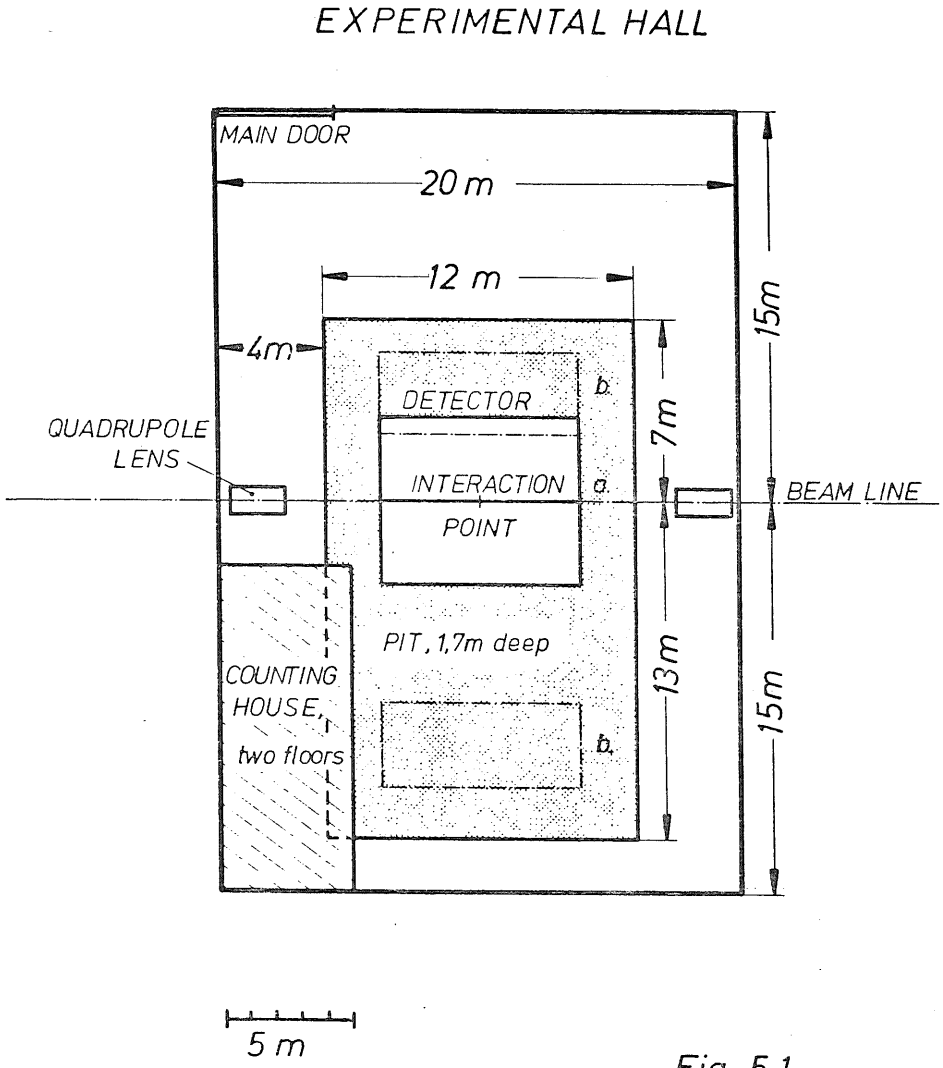

Fig. 5.1

Appendix A

Details of the Construction of the Internal Detector

a) Mechanical.

In each chamber the wires are stretched between two flanges of annular shapes attached to the ends of two concentric cylinders. Chamber 1 is incorporated in the inner cylinder of chamber 2, chamber 5 is incorporated in the outer cylinder of chamber 4. The outer cylinder of each of the three sets can be demounted in sections, giving access to the inside of the chambers.

The flanges are made of Rohacell covered with epoxy fibre-glass plates. The cylinders are made of the same material covered with mylar and aluminum foils. Rohacell is a Plexi-glass foam material of low density (ρ = 0.05 gr/cm^3) with excellent mechanical properties. We have already made drift chambers out of this material for a CERN - experiment.

The anodes will probably be 20 $\mu\phi$ gold plated Tungsten wires. This material is extremely strong (measured breaking force: 90 grams). Its resistivity (200 Ω/m) is sufficient for the determination of the z-coordinate by the charge division method. The potential wires will probably be made of 0.2 mm ϕ metalized Nylon cord. This material is suitable for catching fish of weight up to 24 lbs. The conducting sheet separating the different cells will be made of of carbon-coated aluminized Mylar foil. In order to provide well defined tensions to the wires and foils, these elements will be stretched by individual springs, a technique we have used in all our recent

drift chamber construction. It will probably be necessary to support the anode wire/potential wire systems every 80 cm by very light Rohacell bridges.

The mechanical precision of the wire positions will be limited by the precision of the holes in the flanges, by the wire support system and by the deformation of the wires due to electrical and gravitational forces. We expect to obtain an overall precision of 50 μ or better.

The chamber system is contained in an aluminum vessel constructed to withstand a pressure of 4 Atm (absolute). The outer cylinder has a wall thickness of 1 cm, the inner cylinder will probably be made of a sandwich 0.5 mm Al/8 mm Rohacell/0.5 mm Al. The chamber system is supported by the outer cylinder while the inner cylinder is coupled to the flanges of the aluminium vessel by means of stainless steel bellows. The chamber are accessible for repair through 8 windows in each flange of the pressure vessel. All cables will be brought out through the windows on one side of the tank.

b) Electronics

1) Amplifier system

The amplifier system consists of two preamplifiers and two main amplifiers per chamber wire.

The preamplifier ("VV69") are the same as those already being used in experiments performed by the Heidelberg group at DESY and at CERN.

Their most important characteristies are:

input impedance	50 Ohms
voltage gain	20
rise time	9 nsec
dynamic range	1 : 500
sensitivity	20 μV (i.e 0.4 uA for 50 Ω impedance).
noise (rms)	12 μV

The preamplifiers are mounted inside the pressure vessel and the amplified signals brought out on 3 mm thick coaxial cables.

The main amplifiers are similar to those used in the above mentioned experiments but with larger dynamic range and higher output voltage because the analog memory needs signals up to 5 volts for accurate operation. Therefore, the existing main amplifier system will be modified by adding a power output stage to each amplifier.

2) Track finding logic

It may be necessary to include in the trigger signals from the internal detector indicating the presence of tracks. Such signals can be obtained very easily from the main amplifier output. The amplifiers from all 16 wires of one jet chamber cell are built into one NIM-unit. In this unit a majority coincidence can be demanded, e.g. an 8-fold coincidence with 200 ns time resolution, indicating the presence of a track element pointing to the interaction region.

Several "track-element signals" can then be combined with information from the scintillation counters in an external track finding logic.

3) Jet chamber read out logic

This logic is described in some detail since it is an essential element of the jet chamber system. It consists of:

a) a dual, 8 fold analog memory capable of storing up to 8 successive incoming analog signals from each end of a resistive drift chamber wire and

b) a digital memory driven by a clock for measurement of the time delays of the incoming drift chamber signals.

The digital memory is verified by two Random Access Memories (RAM's) each with a 128 x 1 bit configuration and a specified access time of typically 10 nsec, while the analog memory is built of fast pulse stretchers followed by commercially available sample and hold circuits giving storage times up to some seconds with errors below 1 percent. A simplified block diagram of the logic is shown in Fig. A1 an A2.

There are two modes of operation, "read" and "write". We first consider the write operation (see fig. A1). We assume that additional circuitry provides the "write enable" signals as well as the "write clock" signal related to the instant of beam-beam collision. If now the sum signal from the drift chamber wire exceeds the threshold of the discriminator, a level is set at the "data" inputs of both RAM's and at the "store" inputs of the analog memories.

As a result, the analog inputs of the analog memories are enabled and the first pair of drift chamber signals are stored in the first position of the analog memory. Simultaneously a logical 1 is stored in one of the two RAM's at a position determined by the contents of the "7 bit address counters". Since the "7 bit address counters" are counting a pulse train of constant period, their contents, and hence the address of each RAM, is proportional to the time delay between beam-beam interaction and the arrival of the drift chamber signals.

In order to improve the time resolution to better than the specified value for the memory used (MCM 10147 from Motorola), two RAM IC's are used and clocked with a 180^{o} phase-shifted clock pulse resulting in twice the time resolution of a single IC, i.e. 5 7 ns instead of 10 15 ns. However, to provide this function correctly, additional circuitry is necessary which is not shown in the simplified block diagram for reasons of clarity. (the "read/write enable" signal of the RAM's must be phase related to the "write" clock).

With the trailing edge of the discriminator pulse the "4 bit counter" used for the analog memory address is incremented by 1, allowing the next pair of chamber signals to be stored in the second position of the analog memory.

When the analog memory is completely filled, the overflow signal from the "4 bit counter" is used to inhibit its own clock pulse in order to avoid overwriting of earlier data.

Corresponding to the storage of the analog signals, logical 1's are written into the RAM's defining the time delay of the analog drift chamber signals.

The stored analog and digital information is read out by disabling the "write" and enabling the "read" command. To be sure to start at zero address, a clear signal must be given to all address counters. Then the "read clock" is started and the "7 bit address counters" starts to count up. When the first logical 1 at the data output of one of the RAM's appears, the "read clock" is inhibited and a "read" command is provided for the analog memory. The first pair of drift chamber signals is now multiplexed to the output of the analog memory and fed to an ADC which digitizes both "left" and "right" signals for further compution and storage. (see Fig. A2)

When the ADC is ready after the first pair of conversions it enables the "read" clock again, to allow the next signal pair to be read out in the same way.

Since it is inconvenient to transfer information on each track separately to the computer, a buffer memory stores the information from the ADC as well as that from the RAM's before transmitting it to the computer.

The time information stored as logical 1's in the RAM's is read out by counting the number of "read" clock pulses between the different logical 1's and storing these number in the buffer memory mentioned above from which they can be transmitted to the computer.

The size of the buffer memory depends upon the number of hit wires and the number of hits per wire. Assuming the electronics for 8 wires to be within 1 double width CAMAC module and assuming a word length of 12 bits, which is a convenient length in our case, the maximum number of digital words to be stored is 192 per module. So, on average, a 128 x 12 bit buffer memory should be large enough. Such a memory consists of only 3 IC's.

The most critical part of the drift chamber read out logic is the fast prestretcher in the analog memory because this circuit has to stretch the fast chamber signals from the nanosecond range to a length of several microseconds with an accuracy corresponding to 10 bits. Various FET-stretcher circuits have been built and tested. However, the best solution to this problem has been shown to be a gated stretcher using bipolar transistors (transistor array) as shown in Fig. A3.

High precision electronics

As mentioned above, drift time measurements with high accuracy will be performed for the first particle arriving at each wire of chamber 1 and 5 and at the middle wires of chamber 3. For this measurement commercially available high resolution drift chamber digitiziers will be used. We tested a special version, with 1 nsec bins, of the LeCroy model 2770 for stability and linearity. The tests gave satisfactory results and remained stable for several weeks. Since this unit has some minor disadvantages an improved version which is presently being developed by LeCroy will be used.

Fig. A1 Simplified block diagram of the jet chamber read out logic.

Fig. A2 Simplified block diagram of the jet chamber read out logic. (continued)

Fig. A3 Test results of a fast prestretcher for jet chamber analog signals.

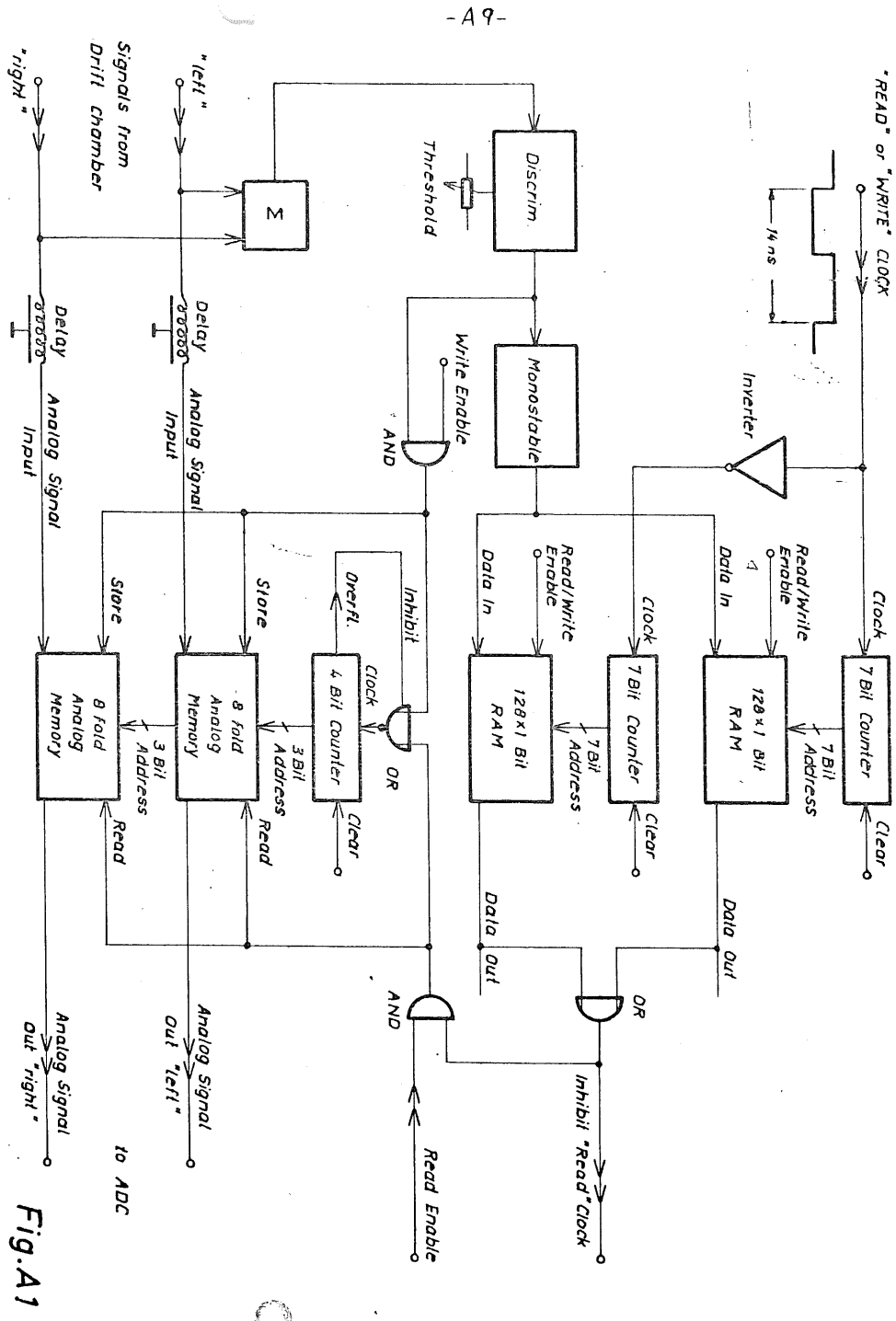

Fig.A1

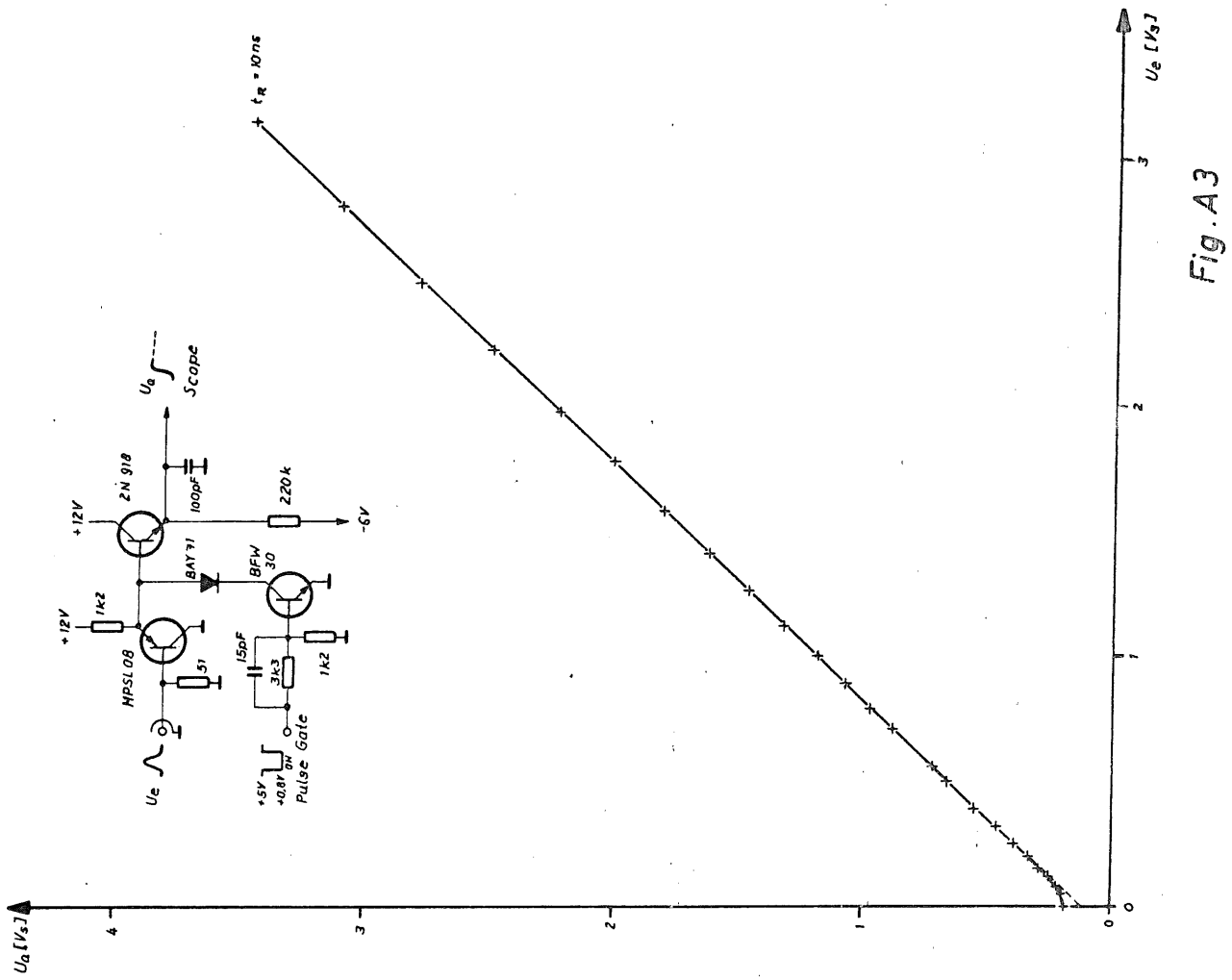

Fig. A3

- A 11 -

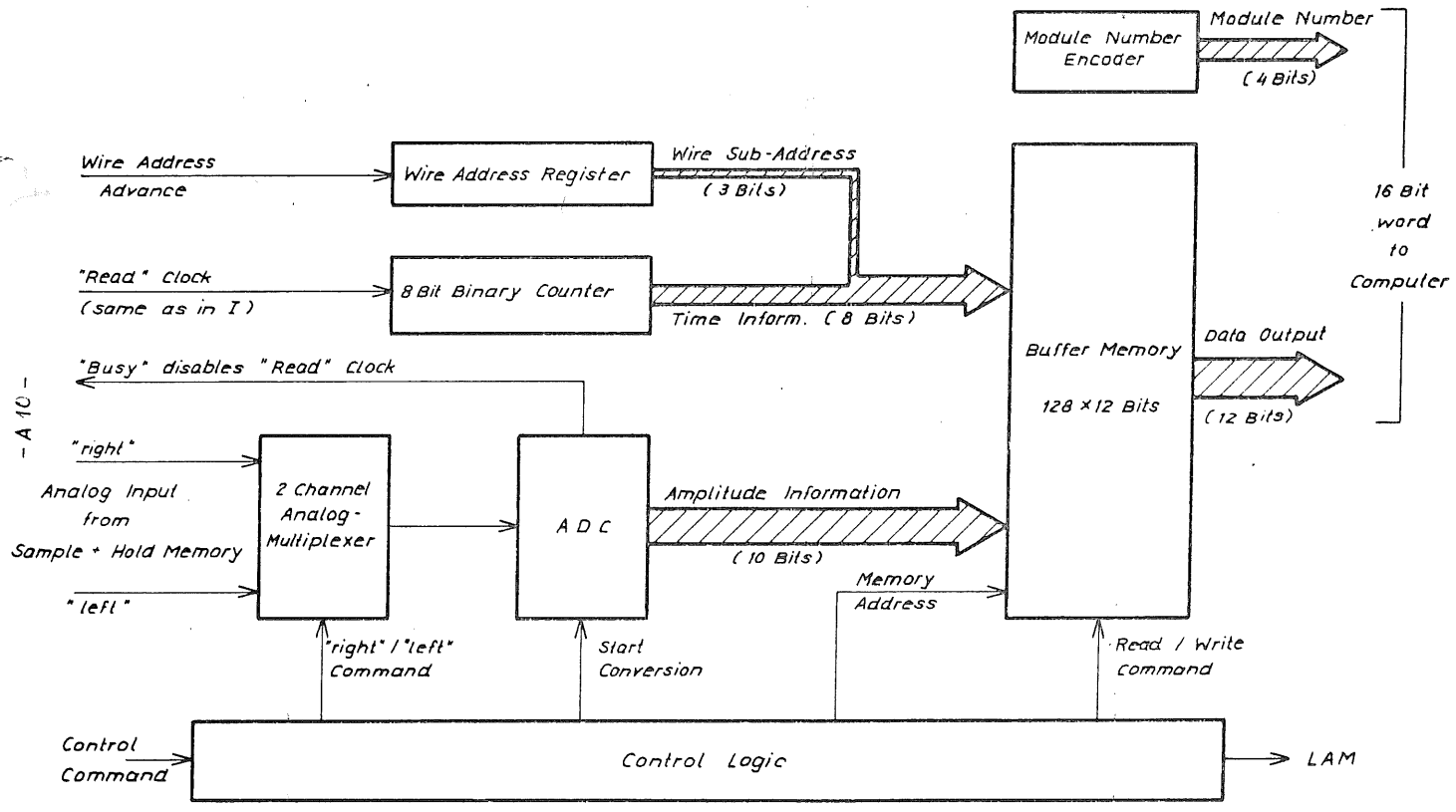

Fig. A2

- A 10 -